An Atomistic Investigation of the Kinetics of Detwinning

Felix E. Hildebrand [a], Rohan Abeyaratne [b,*]

[a] *Center of Mechanics, ETH Zurich, Zurich, Switzerland*

[b] *Department of Mechanical Engineering, Massachusetts Institute of Technology, Cambridge, USA*

Dedicated to James K. Knowles: teacher, colleague and friend.

Abstract

This paper presents a "first principles" atomistic study of the dynamics of detwinning in a shape memory alloy. In order to describe the macroscopic motion of twin boundaries, the *continuum* theory of twinning must be provided with a "kinetic relation", i.e. a relation between the driving force and the propagation speed. This kinetic relation is a macroscopic characterization of the underlying *atomistic processes*. The goal of the present atomistic study is to provide the continuum theory with this kinetic relation by extracting the essential macroscopic features of the dynamics of the atoms. It also aims to elucidate the mechanism underlying the process of detwinning.

The material studied is stoichiometric nickel-manganese, and inter-atomic interactions are described using three physically motivated Lennard-Jones potentials. The effect of temperature and shear stress on detwinning – specifically on the rate of transformation from one variant of martensite to the other – is examined using molecular dynamics. An explicit formula for this (kinetic) relation is obtained by fitting an analytic expression to the simulation results. The numerical experiments also verify that transverse ledge propagation is the mechanism underlying twin-boundary motion. All calculations are carried out in a two-dimensional setting.

Key words: atomistic, molecular dynamics, twinning, kinetic relation, nucleation, shape memory, phase transition, ledge

* Corresponding author.

Email addresses: felixhi@ethz.ch (Felix E. Hildebrand), rohan@mit.edu (Rohan Abeyaratne).

1 Introduction

Certain alloys such as Ni-Ti, Ni-Mn and Cu-Al-Ni possess the capability of recovering from large and seemingly irreversible deformations if heated above a certain threshold temperature. This effect, called the shape memory effect, is possible because such materials are able to transform between two distinct solid phases. At low temperatures, they prefer a crystallographic structure with low-symmetry (e.g. tetragonal) called *martensite*, whereas at high temperatures the stable crystal structure has high-symmetry (e.g. cubic) and is called *austenite*. Each crystallographic structure is said to correspond to a phase of the material.

The low-symmetry phase exists in a number of crystallographically equivalent forms referred to as *variants* (of martensite). In the absence of stress, all of the variants have the same free-energy and are therefore equally stable. Thus different variants can co-exist in a stress-free body; such a configuration is said to be "twinned", a pair of adjacent variants are called "twins", and the kinematically compatible interface between them is called a "twin boundary". Figure 1 shows an atomic scale photograph of a twinned region in a SiC nanoparticle taken from Perrey et al. (2003). When the body is subjected to an applied loading, the free-energies of the different variants are no longer equal and some variants become energetically more favorable than others. Consequently the twin boundaries move into the less favorable variants, thereby transforming them into a more favorable variant. This process can lead to strains of up to $8 - 10\%$.

The transformation between variants at the macroscopic scale, the associated load-deformation curve, the rate effects, and the hysteresis are all controlled by the dynamics of the twinning process. Since this is a non-equilibrium process, it means that the macroscopic response of the material is controlled by ingredients additional to the free-energy that governs the equilibrium response of the material, see e.g. Abeyaratne and Knowles (2006). Specifically, additional information describing the nucleation and motion of interfaces are required, and they must be derived from the dynamics of the transforming lattice (or measured directly from experiments).

Those aspects of the lattice-scale dynamics that are relevant to the macroscopic scale must then be passed up to the *continuum* theory in the form of a "nucleation criterion" and a "kinetic relation". This paper describes an attempt to obtain such information from a "first principles" atomistic study using molecular dynamics. In particular we shall determine the critical shear stress associated with nucleation as a function of temperature, and the transformation rate as a function of both temperature and stress.

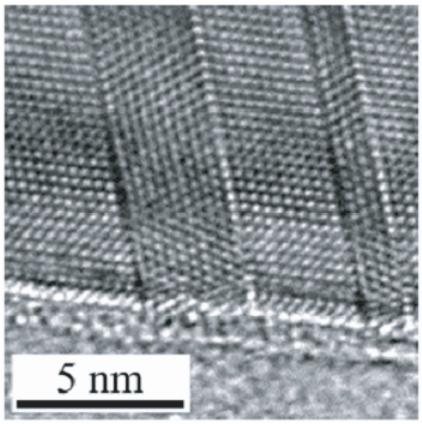

Figure 1. Atomic scale photograph of a twinned microstructure in a SiC nanoparticle, Perrey et al. (2003). Reproduced with permission from C.B. Carter and S.L. Girshick.

The starting point for this work arose from the ideas presented by Kastner (2003, 2006), where he simulated the shape memory effect in a two-dimensional setting using molecular dynamics. The interatomic interactions in his study were modeled employing Lennard-Jones potentials with heuristically constructed parameters. The three primary distinctions between our work and his are that, one, we enforce certain essential group-subgroup lattice symmetry relations (see, e.g. Bhattacharya (2003), Bhattacharya et al. (2004)); two, we use physically motivated values for the Lennard-Jones parameters; and three, our focus is specifically on deriving quantitative descriptions of the nucleation and kinetics of detwinning. In addition, we are also interested in the mechanism by which twin boundaries propagate.

Our molecular dynamics approach is based on (suitable modifications of) the ideas developed by Yip and co-workers for studying structural transformations of lattices, e.g. see Nguyen et al. (1992), Toukan et al. (1983). Related work on the twinning of martensitic lattices have been carried out, for example, by Rifkin and Clapp (1982), Pinsook and Ackland (2000) and Li and E (2005). However, none of them specifically address the questions of nucleation and kinetics. In addition some studies of phase transitions in the literature use interatomic potentials that have multiple energy-wells, thereby building-in the multiple phases into the model a priori. In contrast the interatomic potentials we use have the classical form involving a single energy-well.

The material studied here is stoichiometric nickel-manganese and our analysis is carried out for a two-dimensional lattice. The specimen is a strip that is infinite in one dimension. The outermost atoms of the strip are subjected to shear forces such that the associated continuum may be viewed as being subjected to a uniform shear stress on the straight edges of the strip. A series of calculations are carried out, each corresponding to a different value of force (stress) and different initial kinetic energy (temperature). In particular

we (a) determine bounds on the nucleation level of shear stress as a function of temperature; (b) determine the kinetics of detwinning by calculating the transformation rate as a function of stress and temperature; and (c) examine the forward propagation of an interface and relate it to the transverse propagation of a ledge along the interface.

We note two related recent studies where macroscopic kinetics have been inferred from, in one case a discrete model (Purohit, 2002), and in the other case a continuum model with internal structure (Dayal and Bhattacharya, 2006). In Purohit (2002) a one-dimensional chain of identical particles, each pair characterized by a two-well potential, is considered and the dynamic problem corresponding to holding one end of the chain fixed and moving the other end at a fixed velocity is studied. By examining a number of such problems corresponding to different pulling velocities, the kinetics of the transformation from one well to the other is inferred. The work carried out by Dayal and Bhattacharya (2006) concerns the so-called peridynamic theory of a continuum. Again by studying a dynamic problem for a material characterized by a two-well potential, the authors infer a kinetic relation for the transformation. We note that both these studies introduced a two-well potential at the very beginning as part of their ansatz.

Concerning the motion of ledges noted in item (c) above, a preliminary mechanistic model of this has been described by Hildebrand (2006) based on an appropriate generalization of the classical Frenkel-Kontorowa model of dislocations, (Frenkel and Kontorowa, 1938; Hirth et al., 1982). The motion of ledges has been observed in experiments, e.g. by Bray and Howe (1996), as well as in molecular dynamic studies, e.g. by Li and E (2005). They have been modeled previously using mass-spring models, e.g. by Truskinovsky and Vainchstein (2003), Truskinovsky and Vainchtein (2005), Slepyan et al. (2005), Abeyaratne and Vedantam (1997), Pouget (1991), and also using crystal elasticity, e.g. by Abeyaratne and Vedantam (2003).

The paper is organized as follows: in Section 2 the basic atomistic model is described. In particular we determine the parameters of the three Lennard-Jones potentials that are used to describe nickel-nickel, manganese-manganese and nickel-manganese interatomic interactions. In order to determine the lattice structures allowed by these particular interatomic potentials, in Section 3 we determine the possible equilibrium configurations of the lattice and examine their stability by minimizing the total potential energy of the system. We use molecular statics in this calculation and do not account for thermal vibrations. The results are therefore valid at zero Kelvin only. We find that at this temperature the two-dimensional lattice has access to either of two stable tetragonal martensitic phases or to an unstable cubic austenitic phase.

In order to avoid edge effects in our subsequent molecular dynamic simulations,

it is necessary to orient the lattice correctly relative to the specimen. In Section 4 we therefore examine the kinematics of a configuration that involves two variants of martensite, and calculate the angle that a twin boundary makes with respect to the lattice. This allows us to orient the lattice in our molecular dynamic simulations such that the twin boundary is parallel to the specimen boundaries.

The essential aspects of our molecular dynamic method are described briefly in Section 5. Since we study the response of a specimen in the form of a strip that is infinite in one-dimension, we use fixed periodic boundary conditions in that direction. It is essential that the spacing between a pair of periodic boundaries be chosen correctly if we are to avoid unintended initial stresses. In particular, since we will carry out calculations at various temperatures, it is important that we have an a priori knowledge of the thermal expansion of the lattice; this allows us to chose the spacing, at each temperature, in such a way that no extraneous thermally induced stresses are present. In Section 5.6 we describe how we calculated the thermal expansion using the Parrinello-Rahman method.

Finally in Section 6 we present the results of our molecular dynamic simulations. In particular, Figure 10 shows upper and lower bounds on the nucleation stress at various temperatures. Figure 12 shows a plot of the transformation rate as a function of shear stress at various temperatures; Figure 13 shows the transformation rate as a function of both shear stress and temperature; and equations (37), (38) give an explicit formula for the kinetic relation that fits the simulation data. Finally, Figure 15 shows a sequence of snapshots which show that twin boundary motion is a consequence of transverse ledge propagation.

2 Atomistic Model

The aim of this study is to better understand the mechanisms underlying twin-boundary motion and to calculate a quantitative characterization of the dynamics of detwinning. We seek to do this in the simplest framework that is capable of modeling all of the relevant features without introducing unnecessary parameters and intricacies. In this section we describe the basic ingredients of our atomistic model.

First: Hildebrand (2006) has shown that if the interatomic potential between a pair of atoms has the familiar form involving a single local minimum (energy-well), then the corresponding continuum-scale energy function associated with a mono- or diatomic one-dimensional chain of atoms (a 1-lattice or a 2-lattice) also possesses a *single* energy well. Since multi-well macroscopic potentials are

essential if a continuum theory is to model phase transitions and/or twinning, one concludes that such one-dimensional atomic chains whose interaction is governed by single-well potentials are inadequate for our purposes. This was also found to be true for monoatomic two-dimensional lattices. The simplest system that exhibits a multi-well macroscopic potential is a two-dimensional diatomic lattice as shown schematically in Figure 2. This will be the setting for all further considerations.

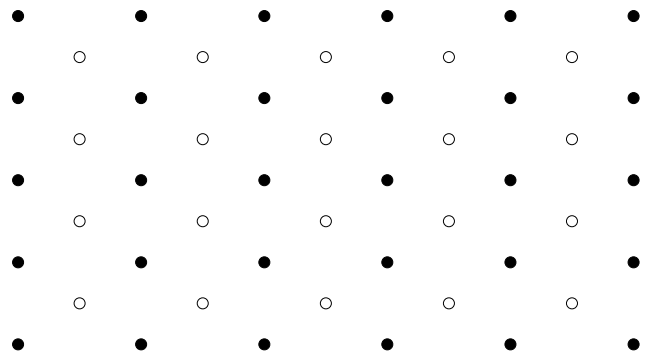

Figure 2. An example of a two-dimensional diatomic lattice. The filled circles represent one atomic species while the open circles represent a different species.

Second: we use the nearly stoichiometric shape memory alloy Ni $-$49at.% Mn as the material in all of our calculations and model it as perfectly stoichiometric. This choice was motivated by the stoichiometry of the material and the simple tetragonal martensitic structure it exhibits. It will become clear in the course of this section why this structure is particularly convenient for our purposes. Other materials that are nearly stoichiometric include Au$-47.5at.\%$Cd, Ni$-49.75at.\%$Ti and CuZr, but they exhibit a more complicated martensitic structure; e.g. see Bhattacharya (2003).

Third: we assume that the Born-Oppenheimer approximation holds and choose pair potentials of the Lennard-Jones form to model interatomic interactions. Although pair potentials are usually used to describe gases and liquids and they overly simplify the interactions in solids, they can frequently capture basic mechanisms and qualitative trends. For example, Elliott et al. (2002) were able to quite accurately predict the stability of different phases in nickel-titanium with temperature-dependent Morse pair potentials. In this paper we choose three Lennard-Jones potentials

$$\Phi^{\alpha\beta}(r) = 4\varepsilon_{\alpha\beta}\left[\left(\frac{\sigma_{\alpha\beta}}{r}\right)^{12} - \left(\frac{\sigma_{\alpha\beta}}{r}\right)^{6}\right], \tag{1}$$

where the potential $\Phi^{\alpha\beta}$ describes the interaction between the atomic species α and β. In the present study, $\alpha\beta$ = NiNi, MnMn, and NiMn.

A setting similar to ours was used previously by Kastner (2003, 2006). However, the interaction parameters $\sigma_{\alpha\beta}, \varepsilon_{\alpha\beta}$ in his work were chosen a priori so

as to yield the desired geometric configurations. As a consequence they do not, for example, satisfy any of the usual combination rules, e.g. the Lorentz-Berthelot rule (Allen and Tildsley, 1987) or the rules proposed by Kong (1973) and Waldman and Hagler (1993). More importantly, the resulting structures do not exhibit the essential group-subgroup relation between the symmetry groups of austenite and martensite; e.g. see Bhattacharya (2003) or Bhattacharya et al. (2004). We circumvent these shortcomings as described below.

The values of the parameters σ_{NiNi} and $\varepsilon_{\mathrm{NiNi}}$ for nickel-nickel interactions were determined by Zhen and Davies (1983) and are given in the second column of Table 1. We were unable to find corresponding values for manganese-manganese interactions in the literature, and so we linearly interpolated the values corresponding to the neighboring elements in the periodic table, viz. chromium and iron, which had also been determined by Zhen and Davies (1983); see third, fourth and fifth columns in Table 1. Finally, to determine the parameters describing nickel-manganese interactions, we applied the Lorentz-Berthelot combination rule (Allen and Tildsley, 1987) leading to the values shown in the last column of Table 1. We also calculated the values of $\sigma_{\mathrm{NiMn}}, \varepsilon_{\mathrm{NiMn}}$ using the two alternative combination rules proposed by Waldman and Hagler (1993) and Kong (1973), but the difference turned out to be negligible (Hildebrand, 2006).

Table 1
Lennard-Jones parameters for nickel-nickel, (chromium-chromium, iron-iron,) manganese-manganese, and nickel-manganese interactions in a three-dimensional lattice; $k_B = 1.38044 \times 10^{-23}$ J/K is Boltzmann's constant.

$\alpha\beta$		NiNi	CrCr	FeFe	MnMn	NiMn
$\sigma^{3D}_{\alpha\beta}$	$\times 10^{-10}$ (m)	2.2808	2.3357	2.3193	2.3275	2.30415
$\varepsilon^{3D}_{\alpha\beta}/k_B$	(K)	6022.3	5789.1	6026.7	5907.9	5964.83

Fourth: A unit cell of the three-dimensional lattice is shown in Figure 3(a). In order to carryout a two-dimensional simulation of this three dimensional lattice, we replaced the actual lattice by the planar one shown in Figure 3(b). The values of the Lennard-Jones parameters of the two-dimensional model are different (but related) to those of the three dimensional model, and they were determined as follows:

It is known from experimental observations that at low temperatures stoichiometric nickel-manganese forms a tetragonal martensitic structure (known as a $\mathrm{L1_0(CuAl)}$ structure; see, e.g. Kren et al. (1967). The nickel atoms form one tetragonal lattice, while the manganese atoms form a second tetragonal lattice that is translated from the nickel lattice. Figure 3(a) displays a unit cell of the three-dimensional lattice with nickel atoms at the vertices of the tetragon

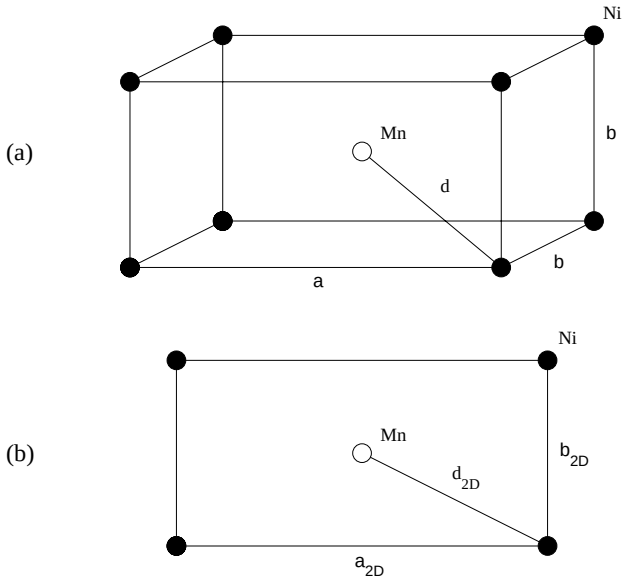

Figure 3. (a) A unit cell of a tetragonal martensite lattice with nickel atoms at the vertices and a manganese atom at the center. (b) The associated two-dimensional lattice.

and a manganese atom at the center. In the absence of thermal vibrations, the lattice parameters are determined by minimizing the potential energy of the crystal. If one minimizes the potential energy of *one* free pair of atoms α and β, then for the Lennard-Jones potential (1) the energy minimizing separation between the two atoms is $2^{1/6}\sigma^{3D}_{\alpha\beta}$. If we use this formula as an estimate for the spacing between *nearest neighbor* atoms, then in the case of the lattice shown in Figure 3(a) we would take

$$b = 2^{1/6}\sigma^{3D}_{\mathrm{NiNi}}, \qquad d = 2^{1/6}\sigma^{3D}_{\mathrm{NiMn}}. \tag{2}$$

Note that the edges of length a do not minimize the energy of the atoms connected by that edge since they are not a nearest-neighbor pair; therefore an equation analogous to (2) is not appropriate for calculating the value of a. Instead from geometry, we have $a = ((2d)^2 - 2b^2)^{1/2}$. Turning to the two-dimensional lattice shown in Figure 3(b), the associated interaction parameters $\sigma^{2D}_{\alpha\beta}, \varepsilon^{2D}_{\alpha\beta}$ and the dimensions b_{2D}, d_{2D}, a_{2D} are similarly related by

$$b_{2D} = 2^{1/6}\sigma^{2D}_{\mathrm{NiNi}}, \qquad d_{2D} = 2^{1/6}\sigma^{2D}_{\mathrm{NiMn}}, \qquad a_{2D} = ((2d_{2D})^2 - b^2_{2D})^{1/2}. \tag{3}$$

If we require the two-dimensional lattice to be the projection of the three-dimensional structure, then the two- and the three-dimensional lattices are related geometrically by $b = b_{2D}$ and $a = a_{2D}$ from which we find using (2) and (3) that

$$\sigma^{2D}_{\mathrm{NiNi}} = \sigma^{3D}_{\mathrm{NiNi}}, \qquad \sigma^{2D}_{\mathrm{NiMn}} \approx 0.868921\sigma^{3D}_{\mathrm{NiMn}}. \tag{4}$$

More precise calculations that took into account more distant neighbors in the lattice were carried out by Hildebrand (2006) yielding $\sigma^{2D}_{\mathrm{NiMn}} \approx 0.864674\sigma^{3D}_{\mathrm{NiMn}}$.

Similarly, by considering a unit cell of the lattice with manganese atoms at the vertices of the tetragon and a nickel atom at the center one finds that $\sigma^{2D}_{\mathrm{MnMn}} = \sigma^{3D}_{\mathrm{MnMn}}$.

Thus in summary, the following parameter values will be used in the Lennard-Jones potential in all calculations pertaining to a two-dimensional lattice:

$$\sigma^{2D}_{\mathrm{NiNi}} = \sigma^{3D}_{\mathrm{NiNi}}, \qquad \sigma^{2D}_{\mathrm{MnMn}} = \sigma^{3D}_{\mathrm{MnMn}}, \qquad \sigma^{2D}_{\mathrm{NiMn}} \approx 0.864674\sigma^{3D}_{\mathrm{NiMn}}, \tag{5}$$

where $\sigma^{3D}_{\mathrm{NiNi}}, \sigma^{3D}_{\mathrm{MnMn}}$ and $\sigma^{3D}_{\mathrm{NiMn}}$ are given in Table 1. Unless explicitly stated otherwise, from hereon we will be concerned exclusively with a two-dimensional lattice; therefore we shall drop the superscript "2D" henceforth.

For numerical purposes, all quantities will be nondimensionalized. To do so, we use the Lennard-Jones parameters of nickel $\sigma_o = \sigma^{3D}_{NiNi}$ for distances; $\varepsilon_o = \varepsilon^{3D}_{NiNi}$ for energies (the numerical values of both σ_o and ε_o are given in Table 1); the unified atomic mass unit $\mu_o = 1.66011 \times 10^{-27} kg$ for masses; and combinations thereof, specifically $T_o = \sqrt{\mu_o \sigma_o^2/\varepsilon_o}$ for time. The nondimensionalized Lennard-Jones parameters thus arrived at for the two-dimensional nickel-manganese system are summarized in Table 2.

Table 2
Modified Lennard-Jones parameters for nickel-nickel, manganese-manganese, and nickel-manganese interactions in nondimensional form for interactions in two dimensions.

$\alpha\beta$	NiNi	MnMn	NiMn
$\sigma_{\alpha\beta}/\sigma_o$	1.0	1.0205	0.8736
$\varepsilon_{\alpha\beta}/\varepsilon_o$	1.0	0.9810	0.9905

In our model we imagine that the two-dimensional planar lattice corresponding to Figure 3(b) is repeated identically on parallel planes in the direction normal to the page. The separation between two adjacent planes is taken to be the lattice spacing b, and during a deformation we assume that all planes deform identically (as in plane strain).

3 Static Analysis

We begin our analysis of the two-dimensional nickel-manganese system by determining the static equilibrium configurations of the system and examining the stability of these structures. This is an essential first step before we account for the additional complexity of temperature.

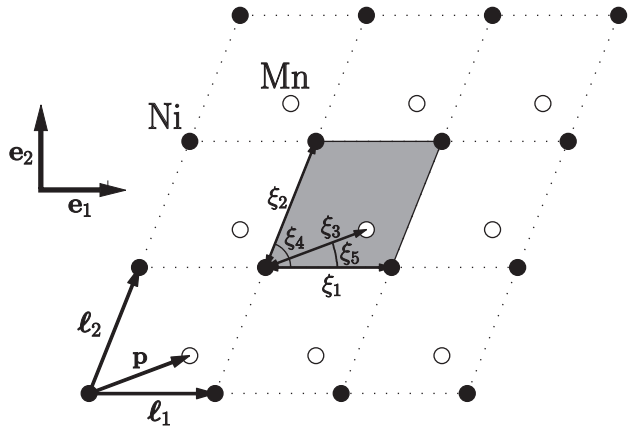

Figure 4. Generalized coordinates $(\xi_1, \xi_2, \xi_3, \xi_4, \xi_5)$ of a two-dimensional diatomic lattice. The shaded region is a unit cell.

The two-dimensional diatomic lattice is a multi-lattice consisting of two simple sublattices that are congruent but shifted with respect to each other; see Figure 4. Each sublattice can be described using the same three generalized coordinates (ξ_1, ξ_2, ξ_4); two additional generalized coordinates (ξ_3, ξ_5) are needed to describe the magnitude and direction of the shift of one sublattice relative to the other. A configuration of the lattice is thus characterized by the vector $\boldsymbol{\xi}$

$$\boldsymbol{\xi} = (\xi_1, \xi_2, \xi_3, \xi_4, \xi_5). \tag{6}$$

Let $\mathbf{e}_1$ and $\mathbf{e}_2$ be a pair of orthonormal unit vectors as depicted in Figure 4. The lattice vectors $(\boldsymbol{\ell}_1, \boldsymbol{\ell}_2)$ of the nickel sublattice, and the shift vector $\mathbf{p}$ of one sublattice relative to the other sublattice are:

$$\boldsymbol{\ell}_1 = \xi_1\, \mathbf{e}_1, \quad \boldsymbol{\ell}_2 = \xi_2(\cos\xi_4\, \mathbf{e}_1 + \sin\xi_4\, \mathbf{e}_2), \quad \mathbf{p} = \xi_3(\cos\xi_5\, \mathbf{e}_1 + \sin\xi_5\, \mathbf{e}_2). \tag{7}$$

If we arbitrarily place the intersection of the zeroth row and the zeroth column of the nickel sublattice at the origin, the position $\mathbf{x}^{\mathrm{Ni}}(m, n)$ of the nickel atom on the mth column and the nth row is

$$\mathbf{x}^{\mathrm{Ni}}(m, n) = m\boldsymbol{\ell}_1 + n\boldsymbol{\ell}_2 \tag{8}$$

where $\mathbf{x}$ denotes the position on a lattice without thermal vibration. Assuming $\xi_3 > 0$ and $\xi_5 < \xi_4$, the position $\mathbf{x}^{\mathrm{Mn}}(m, n)$ of the manganese atom that lies between the mth and $(m+1)$th rows and the nth and $(n+1)$th columns of the nickel sublattice, is

$$\mathbf{x}^{\mathrm{Mn}}(m, n) = \mathbf{x}^{\mathrm{Ni}}(m, n) + \mathbf{p} = m\boldsymbol{\ell}_1 + n\boldsymbol{\ell}_2 + \mathbf{p}. \tag{9}$$

The potential energy of a unit cell (see shaded area in Figure 4) with four nickel atoms at the corners and a manganese atom at the center can now be

calculated. To do so, we add the energy of the manganese atom to one fourth of the sum of the four nickel corner atoms. The energy of each of the atoms is determined accounting for interactions with all like and unlike atoms that are less than or exactly M rows or columns away.

The potential energy of the nickel atom at position $\mathbf{x}^{\mathrm{Ni}}(m,n)$ is then given by

$$U^{\mathrm{Ni}}(\boldsymbol{\xi},m,n) = \sum_{i,j=-M}^{M-1} \frac{1}{2}\Phi^{\mathrm{NiMn}}\Big(|\mathbf{x}^{\mathrm{Ni}}(\boldsymbol{\xi},m,n) - \mathbf{x}^{\mathrm{Mn}}(\boldsymbol{\xi},m+i,n+j)|\Big) + \sum_{\substack{i,j=-M \\ !(i=j=0)}}^{M} \frac{1}{2}\Phi^{\mathrm{NiNi}}\Big(|\mathbf{x}^{\mathrm{Ni}}(\boldsymbol{\xi},m,n) - \mathbf{x}^{\mathrm{Ni}}(\boldsymbol{\xi},m+i,n+j)|\Big). \tag{10}$$

Similarly, the energy of the manganese atom at $\mathbf{x}^{\mathrm{Mn}}(m,n)$ is given by

$$U^{\mathrm{Mn}}(\boldsymbol{\xi},m,n) = \sum_{i,j=-M+1}^{M} \frac{1}{2}\Phi^{\mathrm{NiMn}}\Big(|\mathbf{x}^{\mathrm{Mn}}(\boldsymbol{\xi},m,n) - \mathbf{x}^{\mathrm{Ni}}(\boldsymbol{\xi},m+i,n+j)|\Big) + \sum_{\substack{i,j=-M \\ !(i=j=0)}}^{M} \frac{1}{2}\Phi^{\mathrm{MnMn}}\Big(|\mathbf{x}^{\mathrm{Mn}}(\boldsymbol{\xi},m,n) - \mathbf{x}^{\mathrm{Mn}}(\boldsymbol{\xi},m+i,n+j)|\Big). \tag{11}$$

Combining these, the energy of the unit cell is obtained from

$$U(\boldsymbol{\xi}) = U^{\mathrm{Mn}}(\boldsymbol{\xi},0,0) + \frac{1}{4}\sum_{i,j=0}^{1} U^{\mathrm{Ni}}(\boldsymbol{\xi},i,j), \tag{12}$$

where the choice of $m = 0$ and $n = 0$ is arbitrary. Using the argument of indistinguishability of lattice sites (see, e.g. Pitteri and Zanzotto (2003)), this can be further simplified to

$$U(\boldsymbol{\xi}) = U^{\mathrm{Mn}}(\boldsymbol{\xi},0,0) + U^{\mathrm{Ni}}(\boldsymbol{\xi},0,0). \tag{13}$$

The same result would have been obtained had we chosen a unit cell with manganese atoms in the vertices and a nickel atom in the interior.

To find equilibrium configurations of the lattice we find extrema of the energy U with respect to the generalized coordinates ξ_i by setting

$$\frac{\partial U(\boldsymbol{\xi})}{\partial \xi_i} = 0 \qquad \text{for} \quad \mathrm{i} = 1,2,\ldots,5. \tag{14}$$

Using $M = 5$ in (10) and (11) we carried out the preceding calculation and found three equilibrium structures. The associated values of the parameters $\xi_1, \xi_2, \xi_3, \xi_4$ and ξ_5 are summarized in Table 3. On recalling the geometric significance of the generalized coordinates as shown in Figure 4, we conclude

Table 3
Values of the generalized coordinates associated with the different equilibrium configurations of the two-dimensional nickel-manganese system. For the cubic lattice one usually sets $\xi_1 = a_o$, $\xi_2 = a_o$, whereas for tetragonal variants-1 and -2 one sets $\xi_1 = b$, $\xi_2 = a$ and $\xi_1 = a$, $\xi_2 = b$ respectively.

Parameter	cubic	tetragonal 1	tetragonal 2
ξ_1/σ_o	1.33603	1.14101	1.54110
ξ_2/σ_o	1.33603	1.54110	1.14101
ξ_3/σ_o	0.94472	0.95870	0.95870
ξ_4	$\pi/2$	$\pi/2$	$\pi/2$
ξ_5	$\pi/4$	0.29716	0.20284

that the three equilibrium configurations described in Table 3 correspond to a *cubic* structure and two variants of a *tetragonal* structure.

The values of the two generalized coordinates ξ_1 and ξ_2 at the extrema of U are the lattice parameters of the crystal; see Figures 4. In particular, for the cubic lattice one usually sets $\xi_1 = a_o$, $\xi_2 = a_o$, whereas for the tetragonal variants-1 and -2 one sets $\xi_1 = b$, $\xi_2 = a$ and $\xi_1 = a$, $\xi_2 = b$ respectively.

The lattice parameters a and b for tetragonal Ni-Mn have been experimentally measured by Kren et al. (1967). Since the interaction parameters of our model were constructed such that the two-dimensional lattice was a projection of the three-dimensional nickel-manganese system, it is meaningful to directly compare the calculated values of the lattice parameters a and b presented in Table 3 with the experimentally measured values. At room temperature Kren et al. found $a = 1.543\,\sigma_o$ and $b = 1.159\,\sigma_o$, as opposed to our calculated values

$$a = 1.54110\,\sigma_o, \qquad b = 1.14101\,\sigma_o \tag{15}$$

at 0K according to Table 3. The agreement is rather good and is some indication of the physical relevancy of the simplified model that we have constructed here.

The stability of these equilibrium configurations is determined by the positive definiteness of the Hessian matrix

$$\frac{\partial^2 U(\boldsymbol{\xi})}{\partial \xi_i \partial \xi_j} \tag{16}$$

of the potential energy. Calculating the Hessian and evaluating it at the value of $\boldsymbol{\xi}$ in the second column of Table 3 corresponding to the *cubic* phase leads to a Hessian that is *not* positive-definite. The *cubic* lattice is thus *unstable* at zero absolute temperature. However the Hessian is found to be *positive-definite* when it is evaluated at the values of $\boldsymbol{\xi}$ in the third and fourth columns of Table

3 showing that the two tetragonal lattices are *stable* in the present setting [1] . In addition to this notion of "static stability", "phonon stability" is also necessary for the overall stability of the lattice. We did not investigate this explicitly in this paper but took the fact that the tetragonal structures were observed in the molecular dynamics calculations to be a strong indication of the overall stability of the lattice.

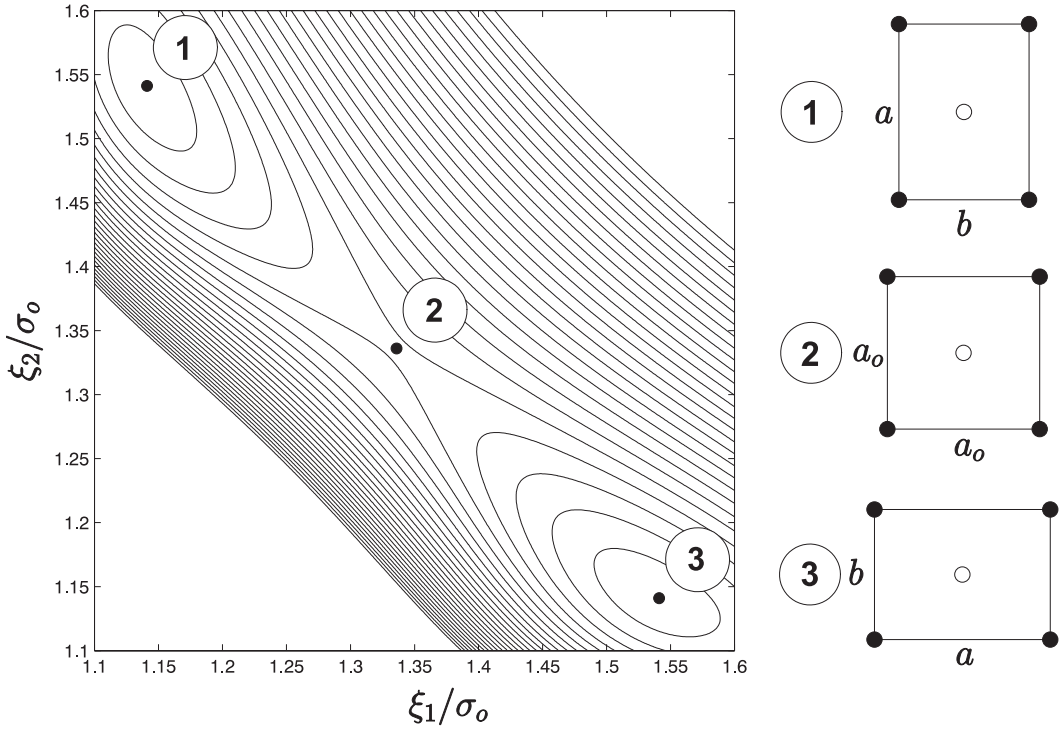

Figure 5. Contour plot of the potential energy $U(\xi_1, \xi_2, \xi_3, \xi_4, \xi_5)$ of the nickel-manganese system on the ξ_1, ξ_2-plane with ξ_3, ξ_4, ξ_5 constrained according to $\xi_3 = \sqrt{\xi_1^2 + \xi_2^2}/2$, $\xi_4 = \pi/2$, and $\xi_5 = \arctan(\xi_2/\xi_1)$. ① and ③ denote minima corresponding to two tetragonal variants, ② corresponds to a cubic configuration.

A contour plot of the energy $U(\xi_1, \xi_2, \xi_3, \xi_4, \xi_5)$ is shown in Figure 5. In order to draw a two-dimensional plot of the energy, we constrained the values of the three parameters ξ_3, ξ_4, ξ_5 and plotted the contours of U on the (ξ_1, ξ_2)-plane; the figure corresponds to the case where the lattice remains rectangular ($\xi_4 = \pi/2$) and the manganese atoms are always located at the center of the nickel cells ($\xi_5 = \arctan(\xi_2/\xi_1)$ and $\xi_3 = \sqrt{\xi_1^2 + \xi_2^2}/2$).

In summary, we conclude from the static analysis that the diatomic two-dimensional nickel-manganese system has the basic properties necesssary for a

[1] It should be mentioned here that our search for minima was by no means exhaustive; there might well be additional extrema at other locations in the five-dimensional parameter space. However in our molecular dynamic simulations the system never "got stuck" (i.e. became equilibrated) in any energy-well other than the two tetragonal ones described previously.

simplified study of twinning: most importantly, there is a low-symmetry, low-temperature martensitic phase that has two variants which are energetically equally favorable under stress-free conditions. This will allow for *twinning* and *detwinning*. Furthermore, a high-symmetry cubic austenitic phase is present but unstable at low temperatures. This phase could potentially be stabilized by entropic effects at higher temperatures (though we have not explored this). Finally, the symmetry group of the austenite and that of the martensite are in a *group-subgroup relation* which is a necessary condition for a material to exhibit the shape-memory effect; see Bhattacharya (2003), Bhattacharya et al. (2004).

4 Twinning of a lattice.

As mentioned in Section 1, our molecular dynamic simulations will be carried out on a horizontal strip of infinite length. Since the crystallographic characteristics of a material determine the orientation of a twin boundary relative to its lattice, and since we want to prevent the twin interfaces from intersecting the boundaries of the specimen, it is necessary that the lattice be suitably oriented relative to the specimen. For this reason, in this section, we briefly review some basic concepts concerning the statics of twinning and apply them to the nickel-manganese system.

A *simple lattice* is given by the infinite collection of points $\mathcal{L}(\boldsymbol{\ell}_1, \boldsymbol{\ell}_2, \boldsymbol{\ell}_3; \mathbf{o})$ obtained from the translation of a basis point $\mathbf{o}$ by whole-numbered multiples of the lattice vectors $\boldsymbol{\ell}_1$, $\boldsymbol{\ell}_2$ and $\boldsymbol{\ell}_3$:

$$\mathcal{L}(\boldsymbol{\ell}_1, \boldsymbol{\ell}_2, \boldsymbol{\ell}_3; \mathbf{o}) = \{\mathbf{x} \,|\mathbf{x} = \mathbf{o} + n_1\boldsymbol{\ell}_1 + n_2\boldsymbol{\ell}_2 + n_3\boldsymbol{\ell}_3, \quad n_1, n_2, n_3 \in \mathbb{Z}\} \tag{17}$$

where $\mathbb{Z}$ is the set of integers. A more complex lattice that consists of two or more simple sublattices, that are either shifted with respect to each other by non-whole-numbered multiples of the lattice vectors or that consist of different kinds of atoms, is called a *multi-lattice*. Specifically, a 2-lattice is a multi-lattice formed of two simple sublattices, each of which is described by the same lattice vectors, and which are translated relative to each other by a shift $\mathbf{p}$. Thus a 2-lattice is the infinite set of points

$$\mathcal{L}(\boldsymbol{\ell}_1, \boldsymbol{\ell}_2, \boldsymbol{\ell}_3; \mathbf{o}) \bigcup \mathcal{L}(\boldsymbol{\ell}_1, \boldsymbol{\ell}_2, \boldsymbol{\ell}_3; \mathbf{o} + \mathbf{p}), \tag{18}$$

where $\mathbf{p}$ is the shift between the sublattices, see Figure 6.

Consider two configurations of a 2-lattice: the first (reference configuration) is characterized by the lattice vectors $\{\boldsymbol{\ell}_1^o, \boldsymbol{\ell}_2^o, \boldsymbol{\ell}_3^o\}$ and shift vector $\mathbf{p}^o$, while the second (deformed configuration) is characterized by lattice vectors $\{\boldsymbol{\ell}_1, \boldsymbol{\ell}_2, \boldsymbol{\ell}_3\}$

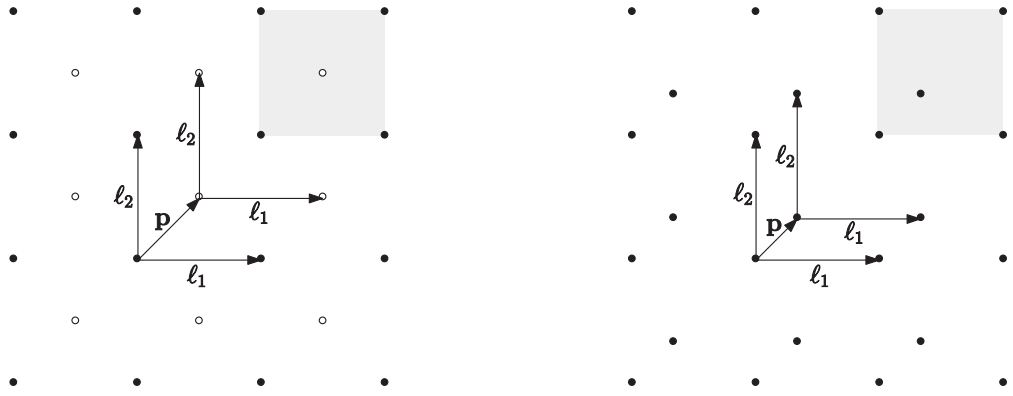

Figure 6. A diatomic 2-lattice (left) and a monoatomic 2-lattice (right) in two-dimensions described by the lattice vectors $\boldsymbol{\ell}_1, \boldsymbol{\ell}_2$ and the shift $\mathbf{p}$. In each case, a unit cell of the lattice is shown shaded. Filled circles represent one atomic species while open circles represent a different species.

and shift vector $\mathbf{p}$. Since lattice vectors are linearly independent, there exists a unique non-singular linear transformation $\mathbf{F}$ that relates them:

$$\boldsymbol{\ell}_i = \mathbf{F}\boldsymbol{\ell}_i^o, \qquad i = 1, 2, 3. \tag{19}$$

By the polar decomposition theorem we can write $\mathbf{F} = \mathbf{R}\mathbf{U}$ where $\mathbf{R}$ denotes a rigid rotation and the symmetric positive definite tensor $\mathbf{U}$ denotes a stretch. If the reference lattice corresponds to unstressed austenite and the deformed lattice corresponds to unstressed martensite, the stretch tensor $\mathbf{U}$ is referred to as the *Bain tensor*.

In the particular case of cubic austenite, with lattice parameters $a_o \times a_o \times a_o$, corresponding lattice vectors $\boldsymbol{\ell}_i^o$ and shift $\boldsymbol{p}_o = \frac{1}{2}(\boldsymbol{\ell}_1^o + \boldsymbol{\ell}_2^o + \boldsymbol{\ell}_3^o)$, and tetragonal martensitic variants with lattice parameters $a \times b \times b$, lattice vectors $\boldsymbol{\ell}_i$ and shift $\boldsymbol{p} = \frac{1}{2}(\boldsymbol{\ell}_1 + \boldsymbol{\ell}_2 + \boldsymbol{\ell}_3)$, there are three possible Bain tensors corresponding to the three possible variants of martensite. The components of these Bain tensors, in an orthonormal basis aligned with the cubic austenite directions, are

$$[\mathbf{U}_1] = \begin{pmatrix} \alpha & 0 & 0 \\ 0 & \beta & 0 \\ 0 & 0 & \beta \end{pmatrix}, \quad [\mathbf{U}_2] = \begin{pmatrix} \beta & 0 & 0 \\ 0 & \alpha & 0 \\ 0 & 0 & \beta \end{pmatrix}, \quad [\mathbf{U}_3] = \begin{pmatrix} \beta & 0 & 0 \\ 0 & \beta & 0 \\ 0 & 0 & \alpha \end{pmatrix}, \tag{20}$$

where the lattice stretches are given by $\alpha = a/a_o$ and $\beta = b/a_o$.

If two variants of martensite, characterized by Bain tensors $\mathbf{U}_I$ and $\mathbf{U}_J$, $I \neq J$, are both present in the same configuration of a body, they are said to form a *twin* and the planar interface between them is called a *twin-interface*, see Figure 7. In the absence of any defects along the interface, the requirement of kinematic compatibility must be satisfied in order to ensure that the lattice is coherent, i.e. given $\mathbf{U}_I$ and $\mathbf{U}_J$, there must exist rotation tensors $\mathbf{R}_I$, $\mathbf{R}_J$; a

vector $\mathbf{a}$; and a unit vector $\hat{\mathbf{n}}$ such that

$$\mathbf{R}_I\mathbf{U}_I - \mathbf{R}_J\mathbf{U}_J = \mathbf{a}\otimes\hat{\mathbf{n}}, \qquad \mathbf{a}\neq\mathbf{0}, \quad |\hat{\mathbf{n}}| = 1, \tag{21}$$

where $\otimes$ represents the dyadic product.

Two implications of the twinning equation (21) are important for our purposes: first, we can write (21) in the form

$$\mathbf{F}_I = (\mathbf{I} + \gamma\hat{\mathbf{a}}\otimes\hat{\mathbf{m}})\mathbf{F}_J \tag{22}$$

where $\mathbf{F}_I = \mathbf{R}_I\mathbf{U}_I, \mathbf{F}_J = \mathbf{R}_J\mathbf{U}_J, \hat{\mathbf{a}} = \mathbf{a}/|\mathbf{a}|, \hat{\mathbf{m}} = \mathbf{F}_J^{-T}\hat{\mathbf{n}}/|\mathbf{F}_J^{-T}\hat{\mathbf{n}}|$ and $\gamma = |\mathbf{a}||\mathbf{U}_J^{-1}\hat{\mathbf{n}}|$. The term in paranethesis on the right hand side of (22) represents a simple shear on a plane normal to $\hat{\mathbf{m}}$, in the direction $\hat{\mathbf{a}}$ by an amount of shear γ; see Figure 7. Therefore the *deformation of the lattice associated with variant-I relative to the lattice associated with variant-J is a particular simple shear*. The unit vector $\hat{\mathbf{m}}$ is said to define the twin plane and the unit vector $\hat{\mathbf{a}}$ defines the twinning direction.

Second, the solution of the twinning equation (21) has been given by Ball and James (1987) as follows: let $\lambda_1, \lambda_2, \lambda_3$ with $\lambda_1 \leq \lambda_2 \leq \lambda_3$ be the ordered eigenvalues of the tensor $\mathbf{U}_J^{-1}\,\mathbf{U}_I^2\,\mathbf{U}_J^{-1} (\neq \mathbf{I})$. Then the twinning equation (21) has a solution if and only if $\lambda_1 \leq 1, \lambda_2 = 1, \lambda_3 \geq 1$, and when these conditions are satisfied, $\hat{\mathbf{n}}$ and $\mathbf{a}$ are given by

$$\begin{aligned}
\hat{\mathbf{n}} &= \frac{\sqrt{\lambda_3}-\sqrt{\lambda_1}}{\rho\sqrt{\lambda_3-\lambda_1}}\left(-\sqrt{1-\lambda_1}\mathbf{U}_J\hat{\mathbf{u}}_1 + \kappa\sqrt{\lambda_3-1}\mathbf{U}_J\hat{\mathbf{u}}_3\right), \\
\mathbf{a} &= \rho\left(\sqrt{\frac{\lambda_3(1-\lambda_1)}{\lambda_3-\lambda_1}}\hat{\mathbf{u}}_1 + \kappa\sqrt{\frac{\lambda_1(\lambda_3-1)}{\lambda_3-\lambda_1}}\hat{\mathbf{u}}_3\right),
\end{aligned} \tag{23}$$

where $\kappa = \pm 1$, ρ is obtained from the normalization $|\hat{\mathbf{n}}| = 1$, and $\hat{\mathbf{u}}_i$ is the unit eigenvector corresponding to the eigenvalue λ_i.

We now apply this result to the two-dimensional nickel-manganese system where we have two variants characterized by the Bain tensors

$$[\mathbf{U}_1] = \begin{pmatrix} \alpha & 0 \\ 0 & \beta \end{pmatrix}, \quad [\mathbf{U}_2] = \begin{pmatrix} \beta & 0 \\ 0 & \alpha \end{pmatrix}. \tag{24}$$

One solution of the corresponding twinning equation $\mathbf{R}\mathbf{U}_2 = \Big(\mathbf{I} + \gamma\hat{\mathbf{a}}\otimes\hat{\mathbf{m}}\Big)\mathbf{U}_1$ is readily found to be

$$\gamma = \frac{\alpha^2-\beta^2}{\alpha\beta}, \tag{25}$$

$$\{\hat{\mathbf{a}}\} = \frac{1}{\sqrt{\alpha^2+\beta^2}}\begin{pmatrix} -\alpha \\ \\ \beta \end{pmatrix}, \qquad \{\hat{\mathbf{m}}\} = \frac{1}{\sqrt{\alpha^2+\beta^2}}\begin{pmatrix} \beta \\ \\ \alpha \end{pmatrix}, \tag{26}$$

where all components are taken with respect to an orthonormal basis $\{\mathbf{e}_1, \mathbf{e}_2\}$ aligned with the cubic austenite axes. The unit normal $\hat{\mathbf{n}}$ to the image of the twin plane in the reference configuration is found to be

$$\{\hat{\mathbf{n}}\} = \begin{pmatrix} 1/\sqrt{2} \\ \\ 1/\sqrt{2} \end{pmatrix}, \tag{27}$$

see Figure 7, while the rotation tensor $\mathbf{R}$ has components

$$[\mathbf{R}] = \begin{pmatrix} \cos\phi & -\sin\phi \\ \sin\phi & \cos\phi \end{pmatrix}, \qquad \tan\phi = \frac{\alpha^2 - \beta^2}{2\alpha\beta}, \qquad \phi \in (0, \pi/2). \tag{28}$$

The numerical values of the stretches α and β may be calculated from the lattice parameter values given in Table 3. They are found to be $\alpha = 1.153492$ and $\beta = 0.85403$.

A geometric interpretation of this solution is depicted in Figure 7. The martensite lattice $\mathcal{L}_1$ is obtained by subjecting the austenite lattice $\mathcal{L}_o$ to a pure stretch $\mathbf{U}_1$. The martensite lattice $\mathcal{L}_2$ can be obtained in either of two equivalent ways: either, by first subjecting the austenite lattice $\mathcal{L}_o$ to a pure stretch $\mathbf{U}_2$ followed by rotating the resulting lattice counter-clockwise by the angle ϕ; or, by subjecting the martensite lattice $\mathcal{L}_1$ to a simple shear of magnitude γ on the plane normal to $\hat{\mathbf{m}}$ in the direction $\hat{\mathbf{a}}$.

When we carry out our molecular dynamic simulations in the following sections, these geometric results inform us on how we should orient the lattice $\mathcal{L}_1$ if we want the twin boundary to be oriented in some specific direction.

A second solution of the twinning equation is given by the symmetric counterpart of the preceding solution.

5 Molecular Dynamic Simulations.

We now carry out molecular dynamic simulations of the nickel-manganese system in order to study the dynamics of the process of detwinning including its thermomechanical complexities. This section outlines some general features of the model and the methods employed including the aspect of thermal expansion; for more details see Hildebrand (2006). The main results of the simulations will be described in Section 6.

We consider a two-dimensional lattice that is infinite in the horizontal direction and has height H in the vertical direction; at the initial instant, the lattice contains a single straight twin boundary a distance h from the bottom as

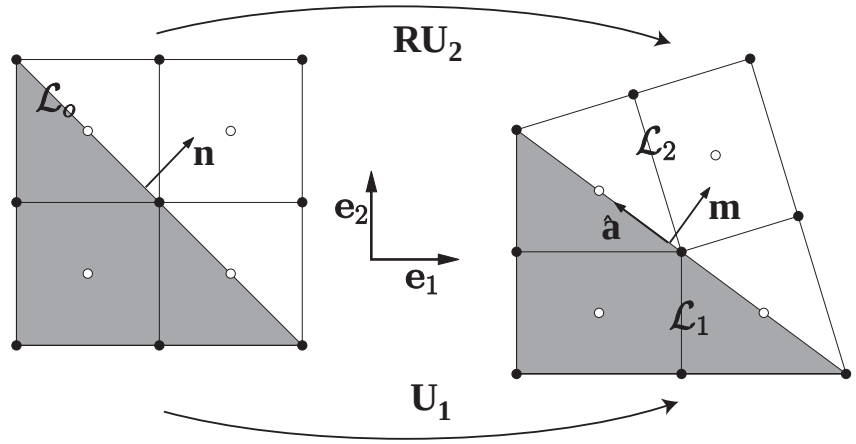

Figure 7. One of the two possible twin-interfaces for nickel-manganese in two dimensions. The unit vectors $\hat{\mathbf{n}}$ and $\hat{\mathbf{m}}$ are normal to the twin boundary in the reference and deformed configuration respectively.

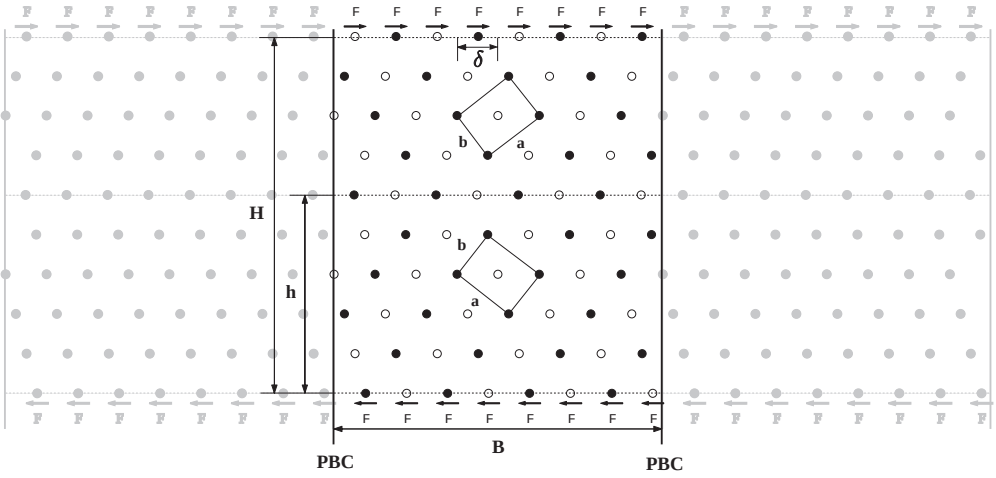

Figure 8. A two-dimensional nickel-manganese lattice of infinite width in the horizontal direction and height H in the vertical direction. Computations are carried out on a cell of dimensions $B \times H$. Periodic boundary conditions (PBC) are applied in the horizontal direction. The lattice involves two martensite variants separated by an interface initially located at a distance h from the bottom. The atoms in the outermost rows are subjected to shear forces F as shown.

depicted in Figure 8. The material above this interface is associated with martensite variant-1 while the material below it is associated with variant-2. Forces, $F > 0$, are applied on each atom of the outermost rows, creating a shear as shown in the figure. Under these conditions, variant-1 is energetically more favorable than variant-2. Consequently, the amount of material associated with variant-1 will increase at the expense of the less favorable variant, variant-2. Our goal is to calculate the rate at which this transformation happens and to observe the mechanism underlying it.

5.1 Equations of Motion.

As discussed previously, despite its drawbacks, we use Lennard-Jones pair potentials $\Phi^{ij}(r)$ to characterize the interaction between the ith and jth atoms. The force on the ith atom due to a surrounding cluster of $N-1$ atoms is

$$\mathbf{F}_i = \sum_{\substack{j=1 \\ j\neq i}}^{N} \left.\frac{\partial \Phi^{ij}(r)}{\partial r}\right|_{r=r_{ij}} \frac{\mathbf{y}_j - \mathbf{y}_i}{r_{ij}}, \qquad r_{ij} = |\mathbf{y}_j - \mathbf{y}_i|, \tag{29}$$

where $\mathbf{y}_i(t)$ is the position of the ith atom at time t during a dynamical process (in contrast to $\mathbf{x}_i$ which referred to a position at a lattice point on a perfect lattice). The equation of motion of this atom is given by Newton's equation:

$$m_i \ddot{\mathbf{y}}_i = \mathbf{F}_i \qquad \text{for all} \quad i = 1, 2, \ldots, N. \tag{30}$$

The masses of the two species of atoms are $m_{\mathrm{Ni}} = 58.69\mu_o$ and $m_{\mathrm{Mn}} = 54.93\mu_o$ where μ_o is the unified atomic mass introduced in Section 2; see Hildebrand (2006).

To permit the use of periodic boundary conditions, and for numerical efficiency, in all our calculations we employ a cut-off radius of $r_c = 4.5\,\sigma_o$. To avoid numerical difficulties associated with discontinuities, the Lennard-Jones potential is replaced in the standard way by a so-called shifted-force Lennard-Jones potential, see for example Berendsen and van Gunsteren (1986). This guarantees the continuous evolution of both the potential energy and the forces in the system.

5.2 Integration of equations of motion.

The equations of motion (30) are integrated using the simple but reliable Verlet algorithm (Verlet, 1967),

$$\mathbf{y}_i^{n+1} = 2\mathbf{y}_i^n - \mathbf{y}_i^{n-1} + \frac{\Delta t^2}{m_i} \sum_{\substack{j=1 \\ j\neq i}}^{N} \left.\frac{\partial \Phi^{ij}(r)}{\partial r}\right|_{r=r_{ij}^n} \frac{\mathbf{y}_j^n - \mathbf{y}_i^n}{r_{ij}^n} + O(\Delta t^4). \tag{31}$$

In order to reduce the computational time associated with keeping track of the atoms that enter and exit the cut-off sphere we use a so-called Verlet neighbor list (Verlet, 1967) with a list radius of $r_l = r_c + \Delta r_c$ and $\Delta r_c = \sigma_o$.

5.3 Periodic boundary conditions.

Due to computational limitations, the size of any simulated system must be limited to a relatively small number of atoms. The implication of this is that either, we can only study very small bodies such as nanocrystals, or, that we can study periodic structures provided we use appropriate periodic boundary conditions (see for example Born and von Karman (1912)). We shall adopt the latter approach. We want to prevent the interaction of the twin interfaces with the boundaries of the body. Since the twin boundary (at least initially) is parallel to the horizontal axis, and because we apply loading on the two outermost rows of atoms, we implement periodic boundary conditions along vertical lines in the body spaced a distance B apart; see Figure 8. In order to prevent the interaction of any atom with its image in neighboring copies of the simulation cell as well as the simultaneous interaction of two copies of an atom with the same third atom, the dimensions of the simulation cell should exceed $2r_c$ – twice the cut-off radius – in the direction of the periodic boundary conditions.

5.4 Thermostat.

In order to simulate isothermal processes, different so-called thermostat algorithms have been suggested in the literature. Among these are the somewhat unphysical rescaling method (e.g. Woodcock (1971)), stochastic approaches where the particles interact with a fictitious heat bath (e.g. Andersen (1980)), extended Hamiltonian approaches which incorporate a degree of freedom representing a surrounding heat bath (e.g. Nosé (1984)), and constraint methods which modify the equations of motion in such a way that kinetic energy is conserved (e.g. Evans (1983), Hoover et al. (1982)). Although we wish to study the kinetics of detwinning at different temperatures, we do not employ a thermostat since its use generally yields physically meaningful results *only* after the system has reached equilibrium. Since we are interested in the dynamic response of the system *during its evolution*, the use of such algorithms is not appropriate for our purposes. By not using a thermostat we derive the advantage of having the correct dynamics during the process but pay the price of having to let the temperature of the system evolve as it wishes to (without, for example, constraining it to be isothermal).

5.5 Initial conditions.

The *macroscopic* system we want to simulate is to be at rest at a temperature θ_o prior to loading. In order for the atomistic system to be in a corresponding

microscopic state, we must first perform a preliminary equilibration calculation. The initial positions of the atoms in this calculation are chosen to coincide with some perfect lattice. If this lattice is taken to be the one that minimizes the energy at zero temperature (as determined by the static analysis of Section 3), large initial stresses will be induced at temperatures in the range of interest to us because the packing of the atoms is too dense and the lattice cannot relax in the direction of the rigid periodic boundaries. Therefore, we instead place the atoms on a uniformly expanded lattice obtained from the zero temperature lattice, where the amount of the (temperature dependent) stretching is calculated using the methods described in Section 5.6 below. Placement of the atoms on the sites of this stretched lattice prevents internal stresses at nonzero temperatures. However, this underestimates the initial value of the potential energy since deviations from the ideal sites due to thermal excitation are neglected. We compensate for this by giving the system an additional amount of initial kinetic energy that transforms to potential energy as the system evolves towards equilibrium. Once in equilibrium, the system has the temperature θ_o, where from statistical mechanics

$$\theta_o = \frac{2K_o}{Nk_B d} \tag{32}$$

where d is the dimension of the system, K_o is the kinetic energy in that state, k_B is Boltzmann's constant and N is the total number of atoms in the simulation cell. In order to prevent a rigid translation of the atoms, initial velocities are assigned such that the resultant momentum of the atoms within the simulation cell is zero. It is not necessary to require that the initial velocities obey a certain distribution (e.g. a Maxwell distribution) since their correlation time with the initial conditions is only a few hundred time steps.

5.6 Thermal expansion.

Here we describe how we calculated the averaged dimensions of the lattice over the temperature range of interest using the so-called Parrinello-Rahman algorithm (Parrinello and Rahman, 1980, 1981). In this method one analyzes a periodically repeating simulation cell that is flexible in *size and shape*. As mentioned above, knowledge of the thermal expansion of the lattice is indispensable when studying the dynamics of detwinning as fixed periodic boundary conditions will be used in the horizontal direction, and the choice of the correct spacing between a pair of periodic boundaries at each temperature level is important in order not to induce unwanted internal stresses.

It should be mentioned at the outset that the Parrinello-Rahman method is based on a Hamiltonian (34) involving ansatz-terms introduced to account for the variability of the simulation cell. As a result it does not describe physically

meaningful dynamical processes of the system. However, once equilibrium is reached, the Parrinello-Rahman system simulates a physically meaningful system (the so-called NPH ensemble) with an accuracy of 3/N, where N is the number of particles in the simulation (800 in our case), see Parrinello and Rahman (1981), Klein (1985). This has been proven for a similar system by Andersen (1980). Since the *only* goal of the present section is the determination of the equilibrium lattice parameters at various temperatures, it is expected that the results of the Parrinello-Rahman algorithm will be accurate.

The basic idea of the method (explained here for a two-dimensional lattice) is the following: Let $\mathbf{h}^1$ and $\mathbf{h}^2$ be vectors that span the simulation cell. If $\mathbf{y}_i$ denotes the position vector of the ith atom in the simulation cell we can write $\mathbf{y}_i = s_i^1\mathbf{h}^1 + s_i^2\mathbf{h}^2 = y_i^1\mathbf{e}^1 + y_i^2\mathbf{e}^2$ where $\{\mathbf{e}^1, \mathbf{e}^2\}$ is a fixed orthonormal basis. Then we have

$$\begin{pmatrix} y_i^1 \\ y_i^2 \end{pmatrix} = \begin{pmatrix} H_{11} & H_{12} \\ H_{21} & H_{22} \end{pmatrix} \begin{pmatrix} s_i^1 \\ s_i^2 \end{pmatrix}, \tag{33}$$

where H_{11}, H_{12} and H_{21}, H_{22} are the components of $\mathbf{h}^1$ and $\mathbf{h}^2$ in the basis $\{\mathbf{e}^1, \mathbf{e}^2\}$. As the simulation cell deforms during a calculation, the positions of the atoms (described by s_i^1 and s_i^2), the vectors $\mathbf{h}^1$ and $\mathbf{h}^2$, and (hence) the components $H_{\alpha\beta}$ of the so-called metric tensor all evolve with time.

In order to account for the variability of the cell geometry, the Parrinello-Rahman method postulates the following extended Hamiltonian:

$$\begin{aligned} \mathcal{H} =& \frac{1}{2}\sum_{i}^{N}\sum_{\substack{j \\ j\neq i}}^{N} \Phi^{ij}(|\mathbf{y}_i - \mathbf{y}_j|) \\ &+ \sum_{i=1}^{N}\frac{1}{2}m_i\left(\sum_{\alpha=1}^{2}\sum_{\beta=1}^{2}\sum_{\gamma=1}^{2} H_{\alpha\beta}H_{\alpha\gamma}\dot{s}_i^{\beta}\dot{s}_i^{\gamma}\right) + \sum_{\alpha=1}^{2}\sum_{\beta=1}^{2}\frac{1}{2}W\dot{H}_{\alpha\beta}\dot{H}_{\alpha\beta} \end{aligned} \tag{34}$$

where Φ^{ij} is the pair potential between the ith and jth atoms. It should be noted that $\frac{1}{2}W\dot{H}_{\alpha\beta}\dot{H}_{\alpha\beta}$ replaces all terms in the Hamiltonian that involve time derivatives of the metric tensor. The equations of motion for the positions of the atoms, as well as for the components of the metric tensor $H_{\alpha\beta}$, are derived from this extended Hamiltonian, e.g. see Toukan et al. (1983) for a similar two-dimensional system. Here W is the fictitious mass of the cell walls and is introduced for purely numerical purposes; its numerical value is usually chosen to be of the same order of magnitude as the mass of an atom.

We applied the Parrinello-Rahman method to the two-dimensional nickel-manganese system to find the equilibrium lattice spacings a and b of the martensitic variants at different temperatures θ_{E}. To do so, an ideal lattice of variant-1 with 800 atoms per simulation cell was equlibrated over $400,000$ time steps. In particular, we took $\Delta t = 0.001\,T_o$ and $W = 250.0\,\mu_o$; the initial lattice spacings for all calculations were chosen to be $a = 1.5383\,\sigma_o$ and

$b = 1.1905\,\sigma_o$, which is slightly larger than their values at absolute zero (see Table 3). Here, and in what follows, we took $\Delta t = T_o/1000$ and note that T_o has the same order of magnitude as the characteristic period of atomic vibrations. The initial kinetic energy was chosen such that the temperature at equilibrium would be close to the desired equilibrium temperature θ_{E}.

The filled squares in Figure 9 show how the thermal expansion of the lattice varies as a function of the temperature. Note that the thermal expansion of the two lattice directions are unequal; in particular the thermal expansion of the larger lattice parameter a (dotted line) is smaller than that of the smaller lattice parameter b (solid line). For purposes of comparison we also carried out an analysis based on classical statistical mechanics as described in Hildebrand (2006), the results of which are depicted by the open squares. Observe that the results from the Parrinello-Rahman simulation show the same trends as the (less accurate) predictions of statistical mechanics.

The figure also illustrates a limitation of our model: as we noted previously our energetic model only involves stable martensite and no stable austenite at zero Kelvin. Kren et al. (1967) have measured two transformation temperatures for the martensite to austenite transformation, 965 K and 1168 K. The thermal expansion graphs in Figure 9 suggest that our model is not able to predict the tetragonal to cubic transformation properly. One of many possible reasons for this could be our projection of all phenomena into two dimensions.

6 Results

We now proceed to study the kinetics of shear-induced detwinning using the set-up shown previously in Figure 8. Consider a two-dimensional strip of nickel-manganese of height H in the vertical direction and infinite length in the horizontal direction. At the initial instant there is a twin boundary at a distance $h = 2H/3$ from the bottom. The regions above and below the interface are composed of martensitic variant-1 and variant-2 respectively, and the associated lattices are oriented appropriately, using the theory outlined in Section 4, to ensure that the twin interface is in the horizontal direction. Forces, $F > 0$, are applied on each atom of the outermost rows in the directions shown in Figure 8. Under these conditions, variant-1 is energetically more favorable than variant-2. Periodic boundary conditions are used in the horizontal direction and a simulation cell has dimensions $B \times H$. Each simulation cell contains a total of 70 rows of atoms, each row involving an alternating arrangement of 20 nickel and 20 manganese atoms. The total number of atoms in a simulation cell is therefore 70×40 atoms.

The first step in each calculation involves equilibrating the unstressed lat-

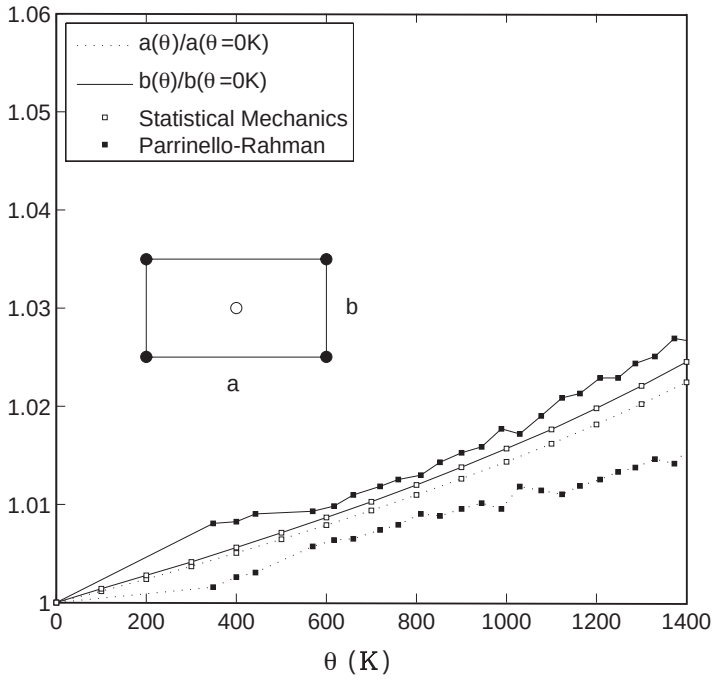

Figure 9. Thermal expansion of the lattice parameters as determined using the Parrinello-Rahman method (filled squares) and statistical mechanics (open squares). Observe that the thermal expansion of a (dotted lines) is smaller than that of b (solid lines).

tice (see also Section 5.5). We do this by carrying out a molecular dynamic simulation over $200,000$ time steps with $\Delta t = 0.001\,T_o$ and $F = 0$. In order to ensure the absence of thermally induced stresses it is essential that the temperature *after* equilibration be close to the temperature corresponding to the chosen spacing of the rigid periodic boundary conditions. This is achieved by supplying the system with additional initial kinetic energy equal to the difference between the equilibrium potential energy obtained from the Parrinello-Rahman simulations and the potential energy of the initial ideal (uniformly thermally expanded) lattice.

The equilibrated system is now sheared by applying constant shear forces F in the range from 0 to $0.030\varepsilon_o/\sigma_o$ as described previously. For each value of force (at each temperature) molecular dynamic simulations are carried out over $300,000$ time steps with $\Delta t = 0.001\,T_o$.

The *applied shear stress* τ on the strip is taken to be the shear force F on each atom divided by the area of the free surface associated with that atom. This area is equal to the length δ (see Figure 8) times the depth b (recall that the distance between atomic planes in the direction perpendicular to the page is b where $a \times b \times b$ are the lattice parameters). Since $\delta = \sqrt{a^2 + b^2}/2$ this yields

$$\tau \;=\; \frac{2F}{b\sqrt{a^2 + b^2}}. \tag{35}$$

6.1 Nucleation.

We find from the calculations that every cell of the lattice remains in its initial variant when the applied shear stress is less than some critical value $\tau_{\rm nuc}$. When the critical shear stress is exceeded, a second twin boundary typically nucleates at the bottom of the specimen (recall that the lower part of the specimen is composed of the energetically less favorable variant). Our calculations yield upper and lower bounds for this critical shear stress [2]. The results are shown in Figure 10 for various initial temperatures. Observe that the threshold value for twinning decreases with increasing temperature.

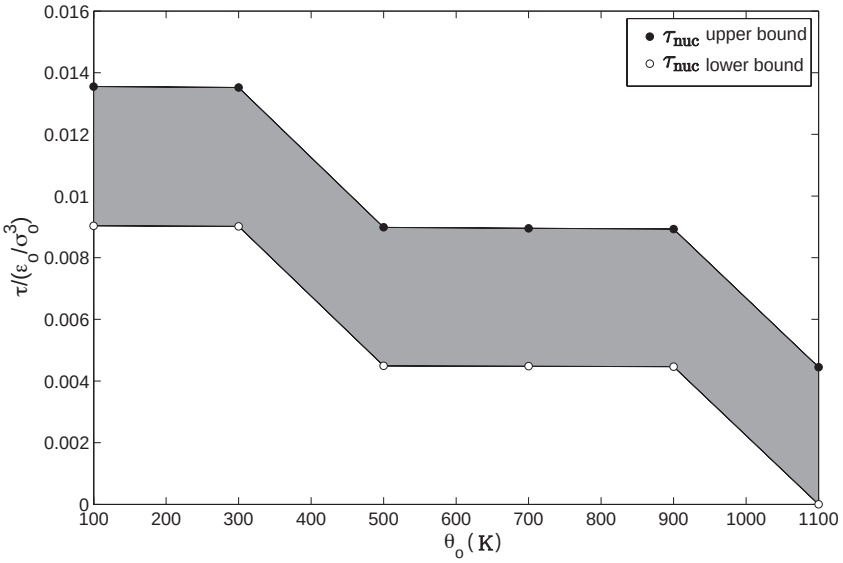

Figure 10. Upper and lower bounds for the critical shear stress $\tau_{\rm nuc}$ for the onset of detwinning at various temperatures θ.

6.2 Transformation kinetics.

When the applied shear stress τ exceeds the nucleation shear stress $\tau_{\rm nuc}$ and the second twin boundary has nucleated, the original and new twin interfaces then

[2] During a calculation we apply a shear stress, say τ_1, and carry out a simulation. Suppose that we find no nucleation. We then apply a higher stress τ_2 and repeat the calculation. Suppose that we now observe nucleation. This does not mean that τ_2 is the nucleation stress. It simply implies that the nucleation stress has some value greater than τ_1 and less than or equal to τ_2. This is why we speak in terms of "upper and lower bounds" on the nucleation stress. Since the increment in shear stress $\tau_2 - \tau_1$ from one calculation to the next was always the same, the curves in Figure 10 are necessarily parallel to each other. This is not a consequence of the physics. The actual nucleation curve could meander between these two bounds.

start to propagate towards each other and the unfavorable variant transforms to the favorable variant. Depending on the value of the applied shear stress, additional layers of the energetically favorable variant may also nucleate and grow in between the approaching boundaries. Figure 11 shows a sequence of snapshots of the specimen during a particular calculation.

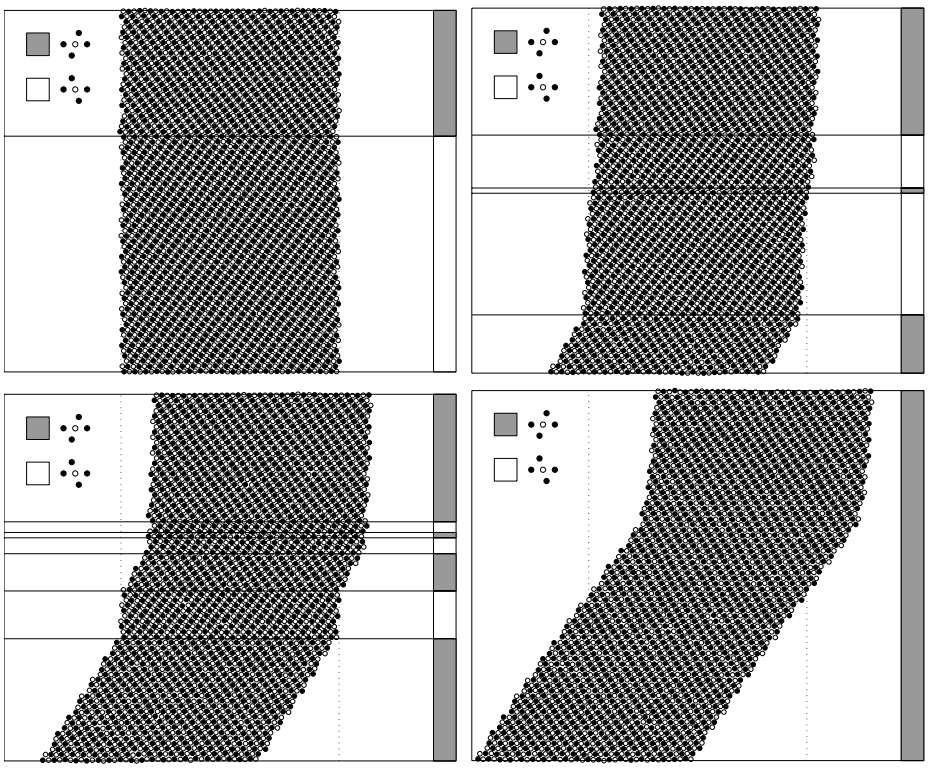

Figure 11. Snapshots at various times during the detwinning process: $t = 0$ (upper left); $t = 100,000\,\Delta t$ (upper right); $t = 200,000\,\Delta t$ (lower left); and $t = 300,000\,\Delta t$ (lower right). In this particular calculation the force on each outermost atom was $F = 0.020\varepsilon_o/\sigma_o$ and the initial temperature was $\theta_o \approx 500K$. The grey and white bar along the right hand vertical edge of each sub-figure provides a measure of the amount of the two variants: the grey segment(s) correspond to the favorable variant, variant-1, and the white segment(s) correspond to variant-2.

Since the transformation involves a number of simultaneously propagating twin-boundaries it is more meaningful to focus on the overall transformation rate in the initially unfavorable part of the simulation cell rather than on the motion of any one specific interface. Let ν denote the rate of change of mass fraction of the favorable variant, or more precisely, the rate of increase of the mass of the favorable variant per unit initial mass of the unfavorable variant. Thus $\nu = \dot{\mathcal{M}}/\mathsf{M}$ where $\dot{\mathcal{M}}$ is the rate of increase of mass of the favorable variant during the simulation and M is the total initial mass of the unfavorable variant (both in a single simulation cell). To calculate ν we use

$$\nu = \frac{\dot{\mathcal{M}}}{\mathsf{M}} = \frac{\mathsf{m} \cdot \mathsf{N}}{\mathsf{M} \cdot \mathsf{n} \cdot \Delta t}, \tag{36}$$

where m is the mass of one row of atoms and n is the number of time steps necessary for the transformation of N rows of atoms.

The transformation rate $\nu = \nu(\tau, \theta)$ from the unfavorable to the favorable variant was calculated through a series of molecular dynamic simulations. For each simulation, a different combination of shear stress τ and initial temperature θ_o was chosen. The transformation rate was averaged over the time from the onset of detwinning to its completion (or the end of the simulation, whichever came first). The corresponding temperature was similarly averaged over the simulation. This is necessary as the temperature of the strip rises (and does not remain uniform) during the detwinning process. In order to do this calculation appropriately without introducing errors due to the kinetic energy associated with the macroscopic shearing motion, the average horizontal velocity of each row of atoms was subtracted from the velocity of its constituents in calculating the temperature using (36).

A plot of the transformation rate ν versus the shear stress τ, at various initial temperatures θ_o, is shown in Figure 12. Observe that $\nu(\tau, \theta_o)$ increases monotonically with τ at each fixed θ_o. Note that this dependence has the approximate square root form $\nu \sim \sqrt{\tau - \tau_c}$. A variety of different square-root forms for kinetic relations at the continuum scale have been developed in the literature, e.g. Abeyaratne et al. (1996), Fath (1998), Abeyaratne and Vedantam (2003), Carpio and Bonilla (2003).

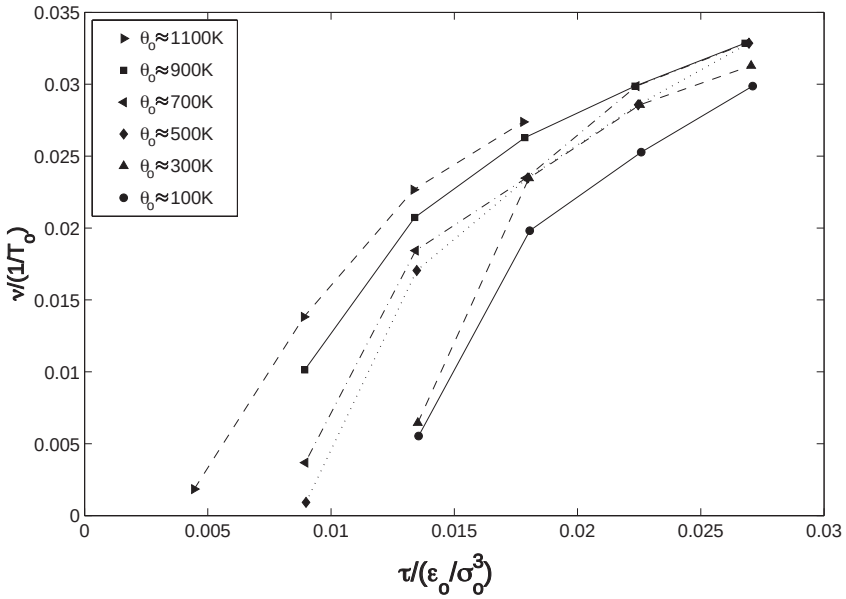

Figure 12. Transformation rate ν as a function of the shear stress τ for different initial temperatures θ_o. The *points* marked on the figure correspond to the results of the molecular dynamic simulations; the straight line segments simply connect these points.

A plot of the transformation rate ν as a function of both the applied shear

stress τ and the average temperature θ is shown in Figure 13 where the points in the figure correspond to the results of the molecular dynamic simulation. Observe that $\nu(\tau, \theta)$ increases monotonically with both τ and θ.

In order to obtain an approximate analytic form for the kinetics, we fit the simulation results to the form

$$\nu(\tau, \theta) = \nu_o \sqrt{\tau - \tau_c(\theta)} \tag{37}$$

using a least squares algorithm and assuming that ν_o was constant and τ_c was linear in θ. In all calculations, the numerical values of the nondimensionalized quantities were used, i.e. τ (and τ_c) had the units ε_o/σ_o^3, θ had units K, and ν (and ν_o) had units $1/T_o$. This led to

$$\nu_o = 0.3718, \qquad \tau_c(\theta) = 0.0136 - 6.8362 \cdot 10^{-6}\theta. \tag{38}$$

A graph of the surface $\nu = \nu(\tau, \theta)$ corresponding to this analytic fit is also shown in Figure 13.

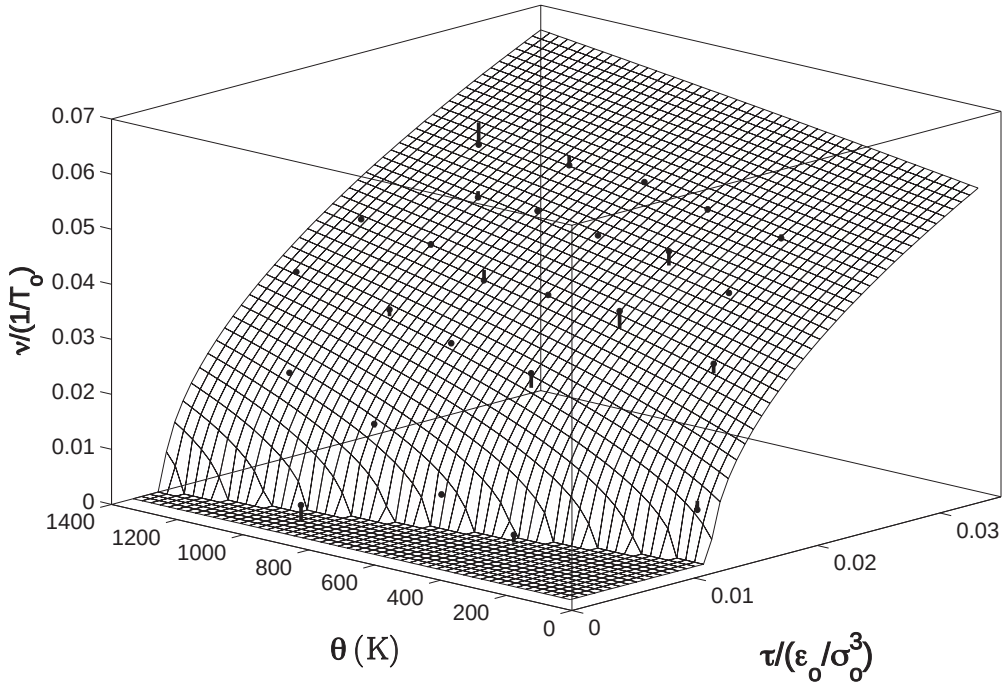

Figure 13. Transformation rate ν as a function of the shear stress τ and the average temperature θ. The points correspond to the results of the molecular dynamic simulations, while the grid represents the analytical approximation $\nu = \nu_o \sqrt{\tau - \tau_c(\theta)}$ given by (37), (38). The vertical bold lines represent the error in the ν-direction between the simulation and the curve fit.

We close this section with a remark about our measure of the transformation rate ν. Note that we calculated the *rate* by averaging over the entire simulation. It is natural to wonder whether this is justified since this effectively assumes a linear evolution of the mass with time during the simulation. Such a measure

of transformation rate would be unsatisfactory if the rate of change of the favorable mass was itself a function of the mass fraction, since in that case the mass fraction would be a nonlinear function of time. In such an event we would have to calculate the transformation rate over every few time steps and consider $\nu = \nu(\tau, \theta, \lambda)$ where the mass fraction $\lambda(t)$ is the ratio of the current mass of the favorable variant to the initial mass of the unfavorable variant; and $\nu = \dot{\lambda}$.

To investigate this we plotted graphs of the mass fraction λ of the favorable variant versus the number of time steps at different temperatures and different force levels. The results are shown in Figure 14. Observe that the evolution of λ is nearly linear in time, thus justifying our approach of averaging over the entire simulation.

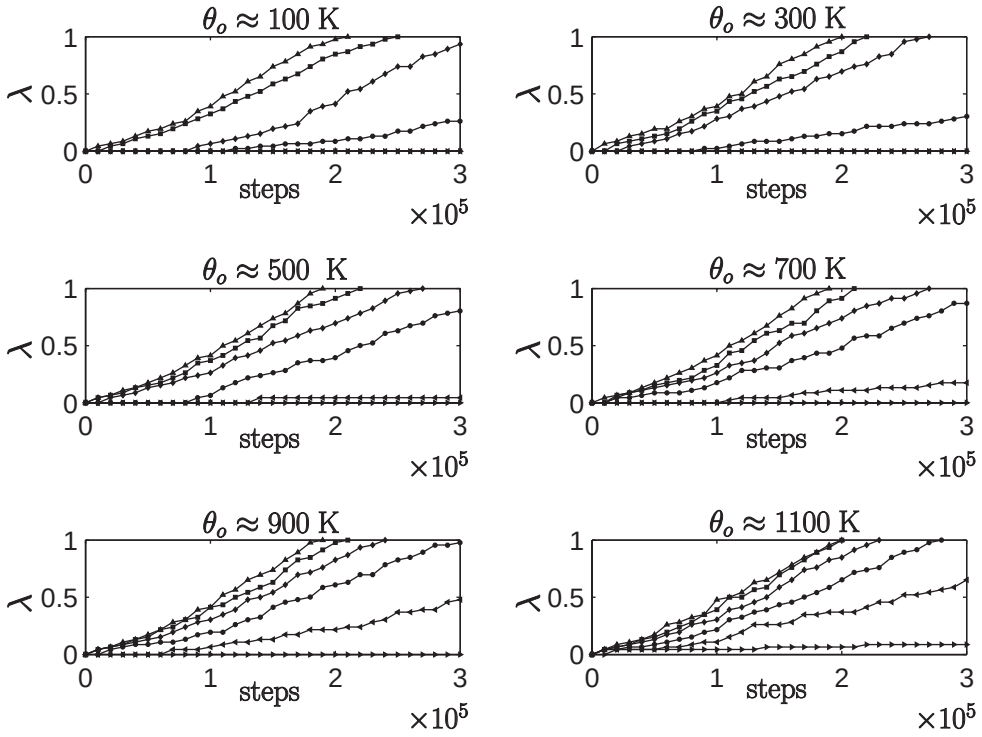

Figure 14. Evolution of the mass fraction λ of the favorable variant versus the number of time steps at different temperatures and different force levels. For each initial temperature θ_o, the different curves represent different levels of applied shear stress using the following symbols. (▶) $\tau = 0.00449\epsilon_o/\sigma_o^3$; (◀) $\tau = 0.00899\epsilon_o/\sigma_o^3$; (●) $\tau = 0.01348\epsilon_o/\sigma_o^3$; (◆) $\tau = 0.01797\epsilon_o/\sigma_o^3$; (■) $\tau = 0.02246\epsilon_o/\sigma_o^3$; and (▲) $\tau = 0.02696\epsilon_o/\sigma_o^3$.

In the preceding subsections we viewed the detwinning transformation at a scale where the transformation evolved through the *forward motion of interfaces* in directions normal to themselves. In this subsection we take a more detailed view, and focus attention on the atoms just ahead of the interface and examine the mechanism by which *each of these atoms individually* transforms from the unfavorable to the favorable variant, which in turn tells us how exactly the twin boundary moves forward.

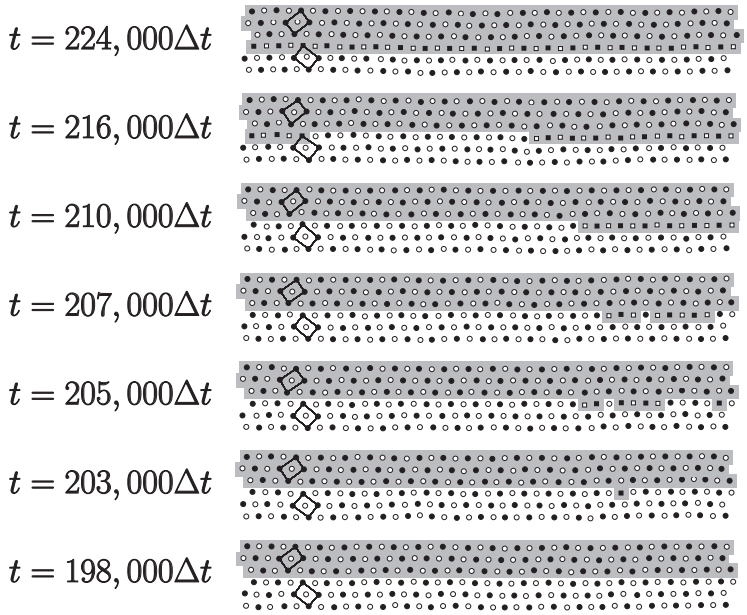

Figure 15. Transformation along a row of atoms; see the text for an explanation of this figure.

Figure 15 shows the transformation along a row of atoms, where the figure is composed of snapshots at seven different time instants during a calculation corresponding to $\theta_o \approx 500K$ and $F = 0.015\varepsilon_o/\sigma_o$. Each snapshot shows rows 43 to 48 (where the 43rd row is at the bottom). Time increases upwards with the bottom snapshot corresponding to $t = 198,000\Delta t$, followed by snapshots at $t = 203,000\Delta t$, $t = 205,000\Delta t$, $t = 207,000\Delta t$, $t = 210,000\Delta t$, $t = 216,000\Delta t$ and ending with the top subfigure corresponding to $t = 224,000\Delta t$. To make the transformation clear, transformed atoms have been placed in a grey background; for both variants, black denotes nickel and white denotes manganese. Additionally, atoms in row 45 that have already undergone the transformation [3] are depicted as squares as opposed to circles.

[3] In order to explain the sense in which we speak of the "transformation of a *single atom*", it is easiest to consider a specific example: consider the one atom that has transformed in row $t = 203,000\Delta t$ in Figure 15 (second row from the bottom). The horizontal position of the transformed atom (black square) is slightly *to the left* of

In this sequence of snapshots it is only the atoms in row 45 that undergo the transformation. At the initial instant every atom in row 45 is untransformed while at the final instant they are all transformed. The sequence of snapshots show how individual atoms on this row transform at different times. From the figure it is clear that the transformation of row 45 occurs one atom at a time. In the case being considered, a single atom transforms (second plot from the bottom) and the transformation propagates in both directions along that row, transversely in the horizontal direction. Due to the periodic boundary conditions, the transformation reenters the simulation cell from the left when it leaves the cell on the right. Over this time period, the twin interface has therefore advanced from row 46 to row 45, and the intermediate snapshots show the detailed process by which this happens.

This mechanism is made even more clear in Figure 16 which shows (the transforming) row 45 only. Each row in the figure corresponds to this same row of atoms but at different times. The bottommost row corresponds to time $t = 199,000\Delta t$ and time increases upwards in increments of 1000 steps. Atoms in the untransformed variant are black, transformed particles are white. The mechanism depicted is often referred to as transformation by the transverse propagation of a "ledge" (or "step") [4] .

As observed previously the transformation proceeds primarily by the nucleation and subsequent propagation of new interfaces rather than by the motion of the pre-existing interface. It is likely that, had we added a pre-existing ledge to the initial interface, that would have facilitated the propagation of the original pre-existing twin boundary. However, since finding the underlying mechanism was one of the questions we wanted to probe, we felt that seeding that particular mechanism with a pre-existing ledge would be favoring one mechanism over other possibilities.

As described in the introduction, such ledges have been previously observed in experiments and molecular dynamic simulations, and have been modeled in various different ways.

---

the closest white atom in the row above it. In the previous snapshot (shown below it and corresponding to $t = 198,000\Delta t$), this atom is positioned *on the right* of this same nearest white neighbor. The black atom has thus *horizontally passed* its nearest neighbor of opposite kind in the row above it. This is what we mean when we speak of the transformation of an atom.

[4] Observe from Figures 15 and 16 that atoms seem to oscillate between two variants before they settle into the new variant. This is an artifact of our definition of a variant in the context of the transformation of a sinlge atom along a row. Since we did not allow for a transition region in our definition, an atom must either be in variant-1 or in variant-2. Simple thermal vibration of an atom can thus lead to an apparent oscillation between the variants.

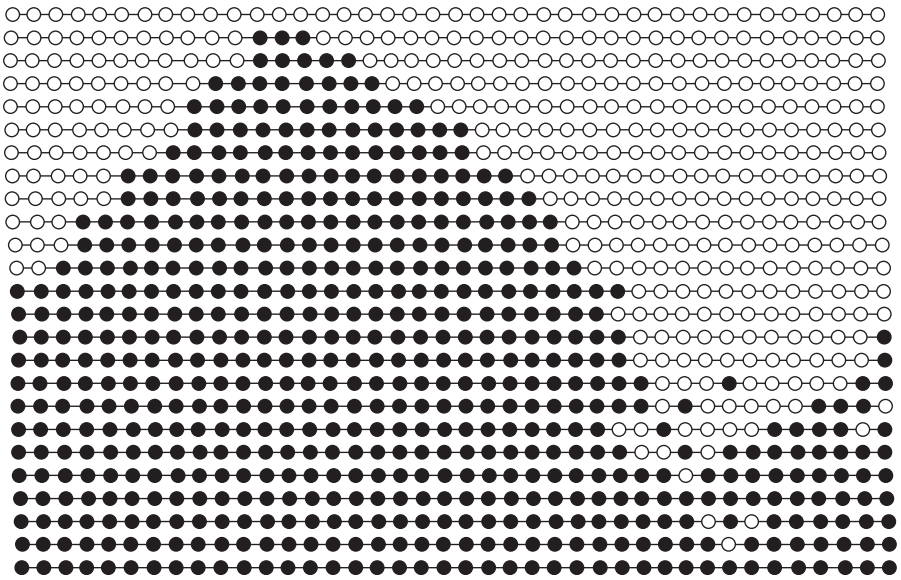

Figure 16. Snapshots of the horizontal positions of the atoms in row 45 during detwinning at $\theta_o \approx 500K$ with $F = 0.015 \cdot \varepsilon_o/\sigma_o$. The bottommost row corresponds to $t = 199,000\Delta t$ and time increases upwards in increments of 1000 steps. The filled circles represent the energetically unfavorable variant, while the open circles denote atoms in the favorable variant.

7 Conclusions

In this paper we have used the methods of molecular dynamics to study the nucleation and kinetics of shear induced detwinning. The goal of our study was to examine these phenomena as a function of temperature and shear stress. The principal results are as follows:

Figure 10 shows upper and lower bounds on the nucleation stress at various temperatures; it shows in particular that the stress-level needed for nucleation decreases with increasing temperature. Figure 12 shows a plot of the transformation rate as a function of shear stress at various temperatures, Figure 13 shows the transformation rate as a function of both shear stress and temperature, and equations (37), (38) give an explicit formula for the kinetic relation that fits the simulation data. They all show that the transformation rate is an increasing function of shear stress and temperature.

Our study also aimed at reaching a better understanding of the underlying microscopic processes and was able to verify the transverse motion of ledges as the mechanism governing twin boundary motion; see Figures 15 and 16.

The analytical form of the kinetic relation obtained here has application more generally in the constitutive modeling of detwinning on the continuum scale. However, it should be kept in mind that the findings here are based on a simplified two-dimensional model. Calculations should be conducted in three

dimensions, and using more sophisticated interaction potentials, to confirm and/or modify the results of this paper. Similar simulations could also be carried out for phase boundary motion.

Acknowledgements

The authors gratefully acknowledge stimulating discussions with Ryan Elliott, Nicolas Hadjiconstantinou and Richard James. Felix Hildebrand wishes to further thank Olaf Weckner, Gerd Brunk and the Dr. Jürgen Ulderup foundation for their support. We thank Professors C.B. Carter and S.L. Girshick for permitting us to reproduce their photograph in Figure 1.

References

Abeyaratne, R., Chu, C., James, R., 1996. Kinetics of materials with wiggly energies: theory and application to the evolution of twinning microstructures in a Cu-Al-Ni shape memory alloy. Philosophical Magazine A 73, 457–497.

Abeyaratne, R., Knowles, J., 2006. Evolution of Phase Transitions: A Continuum Theory. Cambridge University Press.

Abeyaratne, R., Vedantam, S., 1997. Propagation of a front by kink motion - from a discrete model to a continuum model. In: Argoul, P., Fremond, M., Nguyen, Q. (Eds.), Variations of Domains and Free Boundary Problems in Solid Mechanics. Kluwer, pp. 77–84.

Abeyaratne, R., Vedantam, S., 2003. A lattice-based model of the kinetics of twin boundary motion. J. Mech. and Phys. Solids 51, 1675–1700.

Allen, M., Tildsley, D., 1987. Computer Simulation of Liquids. Oxford University Press.

Andersen, H., 1980. Molecular dynamics simulations at constant pressure and/or constant temperature. J. Chem. Phys. 72 (4), 2384–2393.

Ball, J., James, R., 1987. Fine phase mixtures as minimizers of energy. Arch. Rat. Mech. Anal. 100, 13–52.

Berendsen, H., van Gunsteren, W., 1986. Practical algorithms for dynamics simulations. In: Ciccotti, G., Hoover, W. (Eds.), Molecular-Dynamics Simulation of Statistical-Mechanical Systems. North-Holland, pp. 43–65.

Bhattacharya, K., 2003. Microstructure of Martensite: Why it forms and how it gives rise to the shape memory effect. Oxford University Press.

Bhattacharya, K., Conti, S., Zanzotto, G., Zimmer, J., 2004. Crystal symmetry and the reversibility of martensitic transformation. Nature 428, 55–59.

Born, M., von Karman, T., 1912. Über Schwingungen in Raumgittern. Physik. Z. 13, 297–309.

Bray, D., Howe, J., 1996. High-resolution transmission electron microscopy

investigation of the face-centered cubic/hexagonal close-packed martensite transformation in Co-31.8 wt pct Ni alloy: Part 1. plate interfaces and growth ledges. Metallurgical and Materials Transactions A 27A, 3362–3370.

Carpio, A., Bonilla, L. L., 2003. Depinning transitions in discrete reaction-diffusion equations. SIAM J. Appl. Math. 63, 1056–1082.

Dayal, K., Bhattacharya, K., 2006. Kinetics of phase transformations in the peridynamic formulation of continuum mechanics. Journal of the Mechanics and Physics of Solids 54, 1811–1842.

Elliott, R., Shaw, J., Triantafyllidis, N., 2002. Stability of thermally-induced martensitic transformations in bi-atomic crystals. J. Mech. Phys. Solids 50, 2463–2493.

Evans, D., 1983. Computer experiment for nonlinear thermodynamics of Couette flow. J. chem. Phys. 78, 3297–3302.

Fath, G., 1998. Propagation failure of traveling waves in discrete bistable medium. Physica D 116, 176–190.

Frenkel, J., Kontorowa, T., 1938. On the theory of plastic deformation and twinning. Phys. Z. Sowjet Union 13, 1–10.

Hildebrand, F., 2006. Thermomechanical analysis of the kinetics of phase boundaries in shape memory alloys. Master's thesis, Technische Universität Berlin.

Hirth, J., , Lothe, J., 1982. Theory of Dislocations. Wiley, New York.

Hoover, W., Ladd, A., Moran, B., 1982. High strain rate plastic flow studied via nonequilibrium molecular dynamics. Phys. Rev. Lett. 48, 1818–1820.

Kastner, O., 2003. Molecular-dynamics of a 2D model of the shape memory effect - part I: Model and simulations. Continuum Mechanics and Thermodynamics 15 (5), 487–502.

Kastner, O., 2006. Molecular-dynamics of a 2D model of the shape memory effect - part II: thermodynamics of a small system. Continuum Mechanics and Thermodynamics 18 (1-2), 63–81.

Klein, M., 1985. Computer simulation studies of solids. Ann. Rev. Phys. Chem. 36, 525–548.

Kong, C., 1973. Combining rules for intermolecular parameters. II. Rules for the Lennard-Jones (12-6) potential and the Morse potential. J.Chem.Phys. 59 (5), 2464–2467.

Kren, E., Nagy, E., Nagy, I., Pal, L., Szabo, P., 1967. Structures and phase transformations in the Mn-Ni system near equiatomic concentration. J. Phys. Chem. Solids 29 (1), 101–108.

Li, X., E, W., 2005. Multiscale modeling of the dynamics of solids at finite temperature. Journal of the Mechanics and Physics of Solids 53, 1650–1685.

Nguyen, T., Ho, P., Kwok, T., Nitta, C., Yip, S., 1992. Thermal structural disorder and melting at a crystalline interface. Phys. Rev. B. 46 (10), 6050–6060.

Nosé, S., 1984. A molecular dynamics method for simulations in the canonical ensemble. Mol. Phys. 52, 255–268.

Parrinello, M., Rahman, A., 1980. Crystal structure and pair potentials: A

molecular dynamics study. Phys. Rev. Lett. 45 (14), 1196–1199.
Parrinello, M., Rahman, A., 1981. Polymorphic transitions in single crystals: A new molecular dynamics method. J. Appl. Phys. 52 (12), 7182–7190.
Perrey, C., Thompson, R., B., C. C., Gidwani, A., R., M., Renault, T., McMurry, P., Heberlein, J., Girshick, S. L., 2003. Characterization of nanoparticle films and structures produced by hypersonic plasma particle deposition. In: MRS Symp. Proc. Vol. 740. pp. 133–138.
Pinsook, U., Ackland, G., 2000. Atomistic simulation of shear in a martensitic twinned microstructure. Physical Review B 62 (9), 5427–5434.
Pitteri, M., Zanzotto, G., 2003. Continuum Models for Phase Transitions and Twinning in Crystals. Chapman and Hall/CRC.
Pouget, J., 1991. Dynamics of patterns in ferroelastic-martensitic transformations. I. Lattice model. Phys. Rev. B 43, 3575–3581.
Purohit, P., 2002. Dynamics of phase transitions in strings, beams and atomic chains. Ph.D. thesis, California Institute of Technology, Pasadena, California.
Rifkin, J., Clapp, P., 1982. Molecular dynamics studies of martensitic nucleation and growth in two dimensions. J. de Physique 43, 157–162.
Slepyan, L., Cherkaev, A., Cherkaev, E., 2005. Transition waves in bistable structures. II. analytical solution: wave speed and energy dissipation. J. Mech. Phys. Solids 53, 407–436.
Toukan, K., Carrion, F., Yip, S., 1983. Molecular dynamics study of structural instability of two-dimensional lattices. J. Appl. Phys. 56 (5), 1455–1461.
Truskinovsky, L., Vainchstein, A., 2003. Peierls-Nabarro landspace for martensitic phase transitions. Phys. Rev. B 67, 172103.
Truskinovsky, L., Vainchtein, A., 2005. Kinetics of martensitic phase transitions: Lattice model. SIAM J. Appl. Math. 66, 533–553.
Verlet, L., 1967. Computer 'experiments' on classical fluids. I. Thermodynamical properties of Lennard-Jones molecules. Phys. Rev. 159, 98–103.
Waldman, M., Hagler, A., 1993. New combining rules for rare gas van der Waals parameters. J.Comp.Chem. 14 (9), 1077–1084.
Woodcock, L., 1971. Isothermal molecular dynamics calculations for liquid salts. Chem. Phys. Lett. 10, 257–261.
Zhen, S., Davies, G. J., 1983. Calculation of the Lennard-Jones n-m potential energy parameters for metals. Physica Status Solidi A 78 (2), 595–605.